Aerospace Science and Technology 118 (2021) 106992

Contents lists available at ScienceDirect

Aerospace Science and Technology

www.elsevier.com/locate/aescte

Spectral analysis and modelling of the spray liquid injection in a Lean Direct Injection (LDI) gas turbine combustor through Eulerian-Lagrangian Large Eddy Simulations

A. Broatch, M. Carreres *, J. García-Tíscar, M. Belmar-Gil

CMT-Motores Térmicos, Universitat Politècnica de València, Camino de Vera s/n, E-46022, Spain

ARTICLE INFO

Article history:
Received 20 November 2020
Received in revised form 12 July 2021
Accepted 24 July 2021
Available online 3 August 2021
Communicated by Suresh Menon

Keywords:
Gas turbine combustor
Swirling flow
Large Eddy Simulation
Proper Orthogonal Decomposition
Dynamic Mode Decomposition

ABSTRACT

The main challenge of next-generation aeronautical gas turbine engines lies in the increase of the efficiency of the cycle and the reduction of pollutant emissions below stringent restrictions. This has led to the design of new injection-combustion strategies working on more risky and problematic operating points such as those close to the lean extinction limit. In This context, the Lean Direct Injection (LDI) concept has emerged as a promising technology to reduce NOx for future aircraft power plants. The study of liquid fuel injection, atomization, evaporation and later interaction with air by means of a numerical approach is deemed to provide a detailed description of these phenomena affecting the overall engine cycle efficiency and emissions. In this context, the aim of this research is to use Large Eddy Simulation for the characterisation of the structure of a liquid non-reacting spray immersed in a strong swirling field in the CORIA Spray LDI burner. An Eulerian formulation is considered for the continuous phase and is coupled with a Lagrangian description for the dispersed phase. A precise description of the fuel droplet size distribution and size-classified velocity, as well as the characterisation of the instantaneous, mean and fluctuating air velocities is presented and compared to the available experimental data. The fuel spray model is shown to accurately reproduce the computed Sauter Mean Diameter (SMD) and the velocity of the droplets. Moreover, the main flow structures generated within the combustor (e.g., Precessing Vortex Core, Vortex Breakdown Bubble, recirculation zones, etc.), which play a crucial role in the fuel-air mixing process, are quantitatively characterised through advanced frequency analysis such as Proper Orthogonal Decomposition (POD) and Dynamic Mode Decomposition (DMD). The characteristic swirling frequency of a single-branched PVC presenting two different phase-shifted POD modes with the same associated spectrum is detected. Finally, POD and DMD techniques are also applied to the numerical spray data to further investigate the spray-turbulence interactions inside the combustion chamber. In ths regard, DMD analysis has confirmed how the swirl-acoustic interactions led in the VBB and PVC oscillations play a crucial role in the way the fuel spray is internally forced by the PVC wavemaker travelling downstream the swirler and synchronised with its dominant frequency. This will contribute to a better understanding of the mixing quality and local equivalence ratios before the subsequent ignition process.

1. Introduction

The study of advanced aeronautical gas turbine engines is controlled by increasingly stringent environmental regulations, especially NOx [1]. This has led to the design of new injection-combustion strategies working on relatively problematic operating points such as those close to the lean extinction limit. In the case of gas turbine engines used in the aeronautical industry, many advanced ultra-low NOx combustion concepts, such as the Lean Direct Injection concept, are being developed to abide future regulations [2]. However, such systems are more prone to combustion instability if compared to older RQL combustors, which in turn can negatively impact performance and durability. Thus, further investigation in this injection-combustion strategy is required.

In the LDI combustor of the present investigation, the air is swirled upstream of a venturi section, and the liquid fuel is radially injected in spray form into the airstream coming from the venturi throat section in order to produce a lean mixture [3,4]. Hence, atomization, fuel-air mixing, ignition and flame propagation occur in a short period downstream of the injection system, where a high-

* Corresponding author.
E-mail address: marcarta@mot.upv.es (M. Carreres).

https://doi.org/10.1016/j.ast.2021.106992

Nomenclature

List of Notation

$\boldsymbol{a_l}$	liquid phase acceleration vector
B	mass transfer number
C_D	drag coefficient
C_{LISA}	LISA model constant
C_{ps}	empirical constant for the O'Rourke turbulent dispersion model
C_S	Smagorinsky coefficient
C_μ	constant for the mass transport diffusion term
c_l	specific heat of liquid drops
D	diffusion term
D_{ext}	external diameter of the swirler exit (reference length)
D_f	fuel diffusivity
d_0	injector exit diameter
d_D	drop diameter
d_L	ligament diameter
E_i	Relevance of a given DMD mode
e	specific internal energy
e_l	specific internal energy of liquid drops
F^s	rate of momentum increase per unit of volume due to the spray
$F_{d,i}$	sum of drag and gravitational forces on a drop
$F'_{d,i}$	modified sum of drag and gravitational forces on a parcel
f_{grid}	grid-scale factor
$\dot{f}_{bu}$	droplet breakup source term
$\dot{f}_{coll}$	droplet collision source term
g	body forces
h_m	specific enthalpy of species m
K_s	wavenumber corresponding to Ω_s
L_{base}	base cell size
L_{bu}	breakup length
L_{ij}	Leonard stress term
L_{scaled}	scaled cell size
l_v	specific latent heat for vaporisation at constant temperature
M_{ij}	second filtering operation stress term
$\dot{m}_{air}$	supplied air mass flow rate
$\dot{m}_{C_7H_{16}}$	supplied n-heptane mass flow rate
$\dot{m}_l$	liquid mass flow rate
N_p	number of droplets in a parcel
Nu	Nusselt number
Oh	Ohnesorge number
P_{DN}	probable number of droplets
Pr	Prandtl number
p	pressure
p_g	gas pressure
p_v	vapor pressure
$\dot{Q}^s$	source term related to spray interactions
$\dot{Q}_d$	heat flux to a drop
R_{ext}	outer radius of injection
Re	Reynolds number
Re_d	drop Reynolds number
r	radial distance
r_0	drop radius prior to breakup
r_{bu}	breakup radius
r_d	drop radius
S_{ij}	mean strain rate tensor
S_s	work done by turbulent eddies to disperse the liquid spray droplets in a parcel
S_W	swirl number
Sc	Schmidt number
Sh	Sherwood number
T	gas temperature
T_{air}	supplied air temperature
$T_{C_7H_{16}}$	supplied n-heptane temperature
T_D	drop temperature
T_{wall}	wall temperature
t	time
t_d	droplet breakup time
U_{ref}	reference (bulk) velocity at the swirler exit
$\boldsymbol{u}$	velocity vector
$\boldsymbol{u_l}$	liquid phase velocity vector
$u_{l,n}$	velocity component normal to the liquid surface
u_{rel}	relative velocity among droplets
u_{sheet}	liquid sheet velocity
u_z	axial velocity component
u_θ	tangential velocity component
V_c	cell volume
V_d	drop volume
W_g	gas molecular weight
W_v	vapor molecular weight
We	Weber number
$\boldsymbol{x}$	spatial coordinate vector
Y_F	Fuel mass fraction
Y_v	vapor mass fraction in a cell
Y_v^*	vapor mass fraction at the drop surface
y	drop distortion
y^+	non-dimensional boundary layer distance

Greek Symbols

α	heat transfer coefficient
Δ	grid filter
$\hat{\Delta}$	test filter
Δt	time step
Φ_i	DMD spatial modes
X	value of a given variable in the flow field
Ψ_i	POD spatial modes
$\delta_{m,l}$	Kronecker delta function referred to the liquid phase
ε	turbulent dissipation rate
η	liquid surface disturbance displacement
λ	thermal conductivity
λ_{eff}	effective thermal conductivity
μ_l	liquid dynamic viscosity
ν_{coll}	collision frequency of a collector drop
ϕ	swirl vane angle
Ω_s	maximum growth rate
ω	droplet frequency
ρ	density
ρ_g	gas density
ρ_l	liquid density
ρ_m	density of species m
ρ_v	fuel vapor density
$\dot{\rho}^s$	exchange function for the source term due to the evaporation of species
τ	reference time
τ_{PVC}	precession period of the central vortex
τ_{visc}	viscous stress tensor
θ	spray angle

Abbreviations

AMR	Adaptive Mesh Refinement
CFD	Computational Fluid Dynamics
CRZ	Central Recirculation Zone

CTRZ	Central Toroidal Recirculation Zone	POD	Proper Orthogonal Decomposition
DMD	Dynamic Mode Decomposition	PVC	Precessing Vortex Core
LDI	Lean Direct Injection	RMS	Root Mean Square
LES	Large Eddy Simulation	RQL	Rich Burn – Quick Mix - Lean Burn
LDV	Laser Doppler Velocimetry	VBB	Vortex Breakdown Bubble
NMSE	Normalised Mean Square Error		

turbulent recirculation zone is generated as a result of the existing swirling vortex flow.

Even though these flows are employed in most engine designs, their chaotic nature hinders both experimental measurements and numerical computations, implying many issues are still not understood. In the recent past, there have been many experimental and numerical studies regarding different injection strategies (i.e., dual annular -GE DACRS [5], DLR GENRIG [6], BASIS Burner [7]-, twin annular -GE TAPS [8]-, multi-annular -PRECCINSTA [9]-, single -MERCATO [10], GE CFM56 [11], CORIA Burner in unconfined [12–14] and confined [15,16] configurations and HERON [17]-, and multi -NASA LDI [18] and VESTA [19]) and swirler types (i.e., counter-swirl -GE DACRS-, helical -NASA LDI-, cyclone -GE TAPS-, single stage -MERCATO-, dual stage -VESTA-, single-swirl radial KIAI Burner-, and dual-swirl radial -GE CFM56, PRECCINSTA, and DLR GENRIG-).

Experimental observation of spray breakup, mixing and combustion in swirling flows still present some challenges concerning the dense regime, so most of the experimental techniques have been reduced to measurements in the diluted regime employing contrasted techniques such as LDV [20,21], LIF or PDA [22–24]. A vast number of computational research on swirling spray combustors has also been carried out, in part trying to get insight on this dense region. Given the high turbulence and unsteadiness associated to the swirling motion inside the combustor, Large Eddy Simulations (LES) have emerged as a realistic alternative and have been applied in most numerical studies in order to investigate the generation and evolution of fully transient coherent structures in swirl-stabilized combustors [3,25–27]. In LES, the governing equations are filtered to separate the large-scale turbulence, solved by the discretized equation; and small-scale turbulence, modelled through the sub-grid scales models to represent the effects of unresolved small-scale fluid motions. In this way, LES have the potential to provide more accurate representations of the inherently unsteady process of combustion in gas turbine engines in areas such as fuel/air mixing, flame shape and location, and emissions formation.

Concerning the numerical modelling approaches used to simulate multiphase flow systems relevant for conventional swirling spray combustors, the Eulerian-Eulerian (EE), Eulerian-Lagrangian (EL) and hybrid methods should be highlighted. Given that in the Eulerian-Eulerian formulation both carrier and disperse phases are solved using a common Eulerian framework, a consistent numerical method can be used for both phases, thus taking advantage of scalable, high-performance parallel computing [25,28,29]. However, this approach requires substantial modelling effort for the disperse phase and is considered expensive for polydisperse systems. Meanwhile, in the Eulerian-Lagrangian method, the conventional Eulerian framework is used to compute the carrier phase, whereas a Lagrangian tracking is performed for the disperse phase. Despite its slower statistical convergence and inefficient parallelization, this approach is the most common method to simulate swirling spray combustors [30–32] due to its robustness and capability to model complex phenomena such as droplet breakup and interactions. In recent years, hybrid methods have been developed, joining the Eulerian-Eulerian formulation near the nozzle with the Eulerian-Lagrangian approach further downstream to simulate the complete breakup process [33].

The present paper reports a non-reacting LES for the characterisation of the structure of a liquid non-reacting spray immersed in a strong swirling field generated within a radial-swirled lean-direct injection (LDI) combustor. The emphasis of this work is to achieve a precise description of the swirling spray dispersion (e.g., droplet size and size-classified velocity) downstream of the injector, as well as characterising the instantaneous, mean and fluctuating air velocities validating them with available experimental data. A Eulerian-Lagrangian approach is adopted in CONVERGE CFD code to model the fuel injection, atomization, breakup, evaporation and mixing within an automatically generated cartesian mesh with adaptive mesh refinement (AMR) in regions of high gradients in velocity. A drop parcel approximation is considered to statistically represent the entire spray field, significantly reducing the computational resources needed for spray simulations. The selection, calibration and validation of liquid-phase models to predict the spray distribution downstream of the injector have been carried out by applying the methodology established by the authors in previous works. These past studies allowed characterising the flow field with gaseous fuel injections (both in premixed [27] and non-premixed [34] modes) in an LDI burner while optimising the computational resources through several grid control tools. Moreover, the main turbulent flow structures generated within the combustor (e.g., Precessing Vortex Core -PVC-, Vortex Breakdown Bubble -VBB-, recirculation zones, etc.), which play a crucial role in the fuel-air mixing process, are quantitatively characterised through data-driven modal decomposition techniques such as Proper Orthogonal Decomposition (POD) and Dynamic Mode Decomposition (DMD) in an effort to further explain some of the underlying unsteady physics of an LDI combustor. Finally, POD and DMD techniques are also applied to the numerical spray data to further investigate the spray-turbulence interactions inside the combustion chamber. The spectral analysis applied to the disperse phase is expected to shed light in how the swirl-acoustic interactions led by the PVC and VBB oscillations affect the way the fuel spray is dispersed. This will contribute to an in-depth understanding of the mixing quality and local equivalence ratios before the subsequent ignition process. The characterisation of non-reacting instabilities is of primary interest since one of the biggest problems of the LDI technology is the eventual flame blowout [35,36] and the consequent in-altitude re-ignition from a non-reacting field.

The paper is organized as follows. First, a description of the experimental test rig taken as a reference and the operating conditions tested is provided together with a description of the numerical setup and the meshing strategy. Secondly, an analysis of the transient and mean results of gaseous and liquid phases are given. Next, POD and DMD techniques are applied to the numerical gaseous and spray data in order to reveal the self-excited coherent flow structures and its interactions with spray liquid fuel. Finally, the most relevant findings of the investigation are synthesized in the conclusions.

2. Modelling approach

A Lagrangian formulation is used to model the liquid fuel since in the particular application of this investigation (geometry and conditions depicted in Section 2.3) the discrete-particle scales are much smaller (e.g., decens of micrometers) than the smallest turbulent scales solved (e.g., hundreds of micrometers). Additionally, the fuel spray is here described by the injection of a series of discrete liquid parcels containing a certain number of drops, rather than by individual drops. Parcels represent a group of drops (particles) of similar size, location and properties (e.g., velocity, temperature). These drops are collected into single parcels before solving Lagrangian equations for averaged properties of each parcel, thus significantly reducing the computational resources of spray simulations.

2.1. Governing equations

The mass conservation equation for the mixture of gases is described according to Eq. (1):

$$\frac{\partial \rho_m}{\partial t} + \nabla \cdot (\rho_m \boldsymbol{u}) = \nabla \cdot \left[\rho D \nabla \cdot \left(\frac{\rho_m}{\rho} \right) \right] + \dot{\rho}^s \delta_{m,l} \tag{1}$$

where ρ_m is the mass density of species m, ρ is the total mass density and $\dot{\rho}^s \delta_{m,l}$ corresponds to the source term due to the evaporation of the species, where $\delta_{m,l}$ is the Kronecker delta function referred to the liquid phase.

The momentum conservation equation for the fluid mixture including the turbulence modelling can be expressed according to Eq. (2):

$$\frac{\partial \rho \boldsymbol{u}}{\partial t} + \nabla \cdot (\rho \boldsymbol{u}\boldsymbol{u}) = -\nabla p - \nabla \left(\frac{2}{3} \rho k \right) + \nabla \tau_{visc} + F^s + \rho g \tag{2}$$

where τ_{visc} is the total (laminar and turbulent) viscous stress tensor, F^s is the rate of momentum increment per unit of volume due to the spray and g is the body force, which is assumed to be constant. The viscous stress tensor can be related to the diffusion coefficient D and written in Newtonian form according to Eq. (3):

$$\tau_{visc} = \rho D \left[\left(\nabla \boldsymbol{u} + \nabla \boldsymbol{u}^T \right) - \frac{2}{3} \nabla \cdot \boldsymbol{u} \boldsymbol{I} \right] \tag{3}$$

where $\boldsymbol{I}$ is a unit dyadic.

The energy conservation equation, in turn, is described as per Eq. (4):

$$\frac{\partial \rho e}{\partial t} + \nabla \cdot (\rho \boldsymbol{u} e) = -p \nabla \cdot \boldsymbol{u} - \nabla \cdot J + \rho \varepsilon + \dot{Q}^s \tag{4}$$

where $\dot{Q}^s$ is the source term related to spray interactions. The effects of turbulent heat conduction and enthalpy diffusion are considered in the heat flux vector J, which can be expressed according to Eq. (5):

$$J = -\lambda \nabla T - \rho D \sum_m h_m \nabla \cdot \left(\frac{\rho_m}{\rho} \right) \tag{5}$$

where λ is the thermal conductivity, T is the gas temperature and h_m is the specific enthalpy of species m.

The diffusion term D in the transport of mass, momentum and energy is related to the transport of turbulent kinetic energy k and its corresponding dissipation rate ε as given by Eq. (6):

$$D = C_\mu \frac{k^2}{\varepsilon} \tag{6}$$

where C_μ is a constant that needs to be modelled, together with k and ε, by means of a turbulence model.

The governing equation for the discrete phase, also known as spray equation [37], describes the evolution of the droplet distribution through a function f that represents the probable number of droplets P_{DN} according to Eq. (7):

$$P_{DN} = f(\boldsymbol{x}, r_d, \boldsymbol{u_l}, T_d, y, \dot{y}, t)\, \mathrm{d}\boldsymbol{x} \mathrm{d}r_d \mathrm{d}\boldsymbol{u_l} \mathrm{d}T_d \mathrm{d}y \mathrm{d}\dot{y} \tag{7}$$

where r_d is the drop radius, T_d is the drop temperature, y the drop distortion and $\dot{y}$ the drop distortion rate. The time rate of change of the distribution function f can be obtained by solving a Taylor series expansion form of the spray equation, which reduces grid effects on the spray:

$$\frac{\partial f}{\partial t} + \nabla_x \cdot (f \boldsymbol{u_l}) + \nabla_u \cdot (f \boldsymbol{a_l}) + \frac{\partial (f \dot{r}_d)}{\partial r_d} + \frac{\partial \left(f \dot{T}_d \right)}{\partial T_d} + \frac{\partial (f \dot{y})}{\partial y} + \frac{\partial (f \ddot{y})}{\partial \dot{y}} = \dot{f}_{coll} + \dot{f}_{bu} \tag{8}$$

where the quantities $\boldsymbol{a_l}$, $\dot{r}_d$, $\dot{T}_d$ and $\ddot{y}$ are the time rates of changes of liquid velocity, radius, temperature and oscillation velocity ($\dot{y}$) of an individual droplet, respectively. Meanwhile, the source terms $\dot{f}_{coll}$ and $\dot{f}_{bu}$ are originated from droplet collision and breakup, respectively.

By solving the spray equation, the exchange functions $\dot{\rho}^s$, F^s and $\dot{Q}^s$ for liquid-gas coupling can be calculated by summing the rate of mass, momentum and energy for all the drops existing in the spray at position $\boldsymbol{x}$ and time t:

$$\dot{\rho}^s = -\int f \rho_l 4\pi r^2 \dot{r} \mathrm{d}\boldsymbol{u_l} \mathrm{d}r_d \mathrm{d}T_d \mathrm{d}y \mathrm{d}\dot{y} \tag{9}$$

$$F^s = -\int f \rho_l \left(\frac{4}{3} \pi r^3 \boldsymbol{a}' + 4\pi r^2 \dot{r} \boldsymbol{u_l} \right) \mathrm{d}\boldsymbol{u_l} \mathrm{d}r_d \mathrm{d}T_d \mathrm{d}y \mathrm{d}\dot{y} \tag{10}$$

$$\dot{Q}^s = -\int f \rho_l \left\{ 4\pi r^2 \dot{r}_d \left[e_l + \frac{1}{2} (\boldsymbol{u_l} - \boldsymbol{u}) \right] + \frac{4}{3} \pi r^3 \left[c_l \dot{T}_d + \boldsymbol{a}' (\boldsymbol{u_l} - \boldsymbol{u} - \boldsymbol{u}') \right] \right\} \mathrm{d}\boldsymbol{u_l} \mathrm{d}r_d \mathrm{d}T_d \mathrm{d}y \mathrm{d}\dot{y} \tag{11}$$

where e_l and c_l are the specific internal energy and specific heat of liquid drops, respectively. The term $(\boldsymbol{u_l} - \boldsymbol{u})$ corresponds to the relative velocity between the liquid droplet and gas, whereas $\boldsymbol{u}'$ corresponds to the turbulent velocity fluctuations of the gas phase.

The velocity of a single drop $(u_{l,i})$ is obtained from its equation of motion:

$$\rho_l V_d \frac{\mathrm{d}u_{l,i}}{\mathrm{d}t} = F_{d,i} = C_D \pi r^2 \frac{\rho_g \left| u_g - u_{l,i} \right|}{2} \left(u_g - u_{l,i} \right) + \rho_l V_d g_i \tag{12}$$

where V_d is the drop volume and C_D is its drag coefficient. The right-hand side of Eq. (12) is the sum of forces on the drop $F_{d,i}$, whose two terms correspond to the drag and gravitational forces on the drop, respectively.

2.2. Relevant submodels

2.2.1. Turbulence modelling

The Dynamic Smagorinsky LES sub-grid scale model has been applied for the treatment of turbulence to characterize the unsteady non-reacting flow field. In this submodel, the sub-grid scale tensor is given by Eq. (13) [38]:

$$\tau_{turb,ij} = -2C_S^2 \Delta^2 \overline{S}_{ij} \sqrt{S_{ij} S_{ij}} \tag{13}$$

where Δ is the grid filter (related to the cell volume V_c as $\Delta = \sqrt[3]{V_c}$) and C_S is the Smagorinsky coefficient, which is dynamically adjusted locally according to Eq. (14) [39]:

$$C_S = \frac{M_{ij}L_{ij}}{M_{kl}M_{kl}} \tag{14}$$

where L_{ij} is the Leonard stress term and M_{ij} accounts for a second filtering operation through a test filter $\hat{\Delta} = 2\Delta$. For more details on the Dynamic Smagorinsky sub-grid scale model, the reader is referred to Germano et al. [39].

It is important to note that this sub-grid scale model has been chosen according to the conclusions extracted from a previous study about the influence of LES sub-models in a gaseous-fuelled LDI case [27], where its performance for a gaseous-fuelled case was assessed against the use of the Smagorinsky and Dynamic Structure models and the computation of LES quality indexes was found adequate according to the criteria by Pope [40] and Celik et al. [41].

2.2.2. Atomization and breakup modelling

Section 2.4 will describe the two simulations performed for the present investigation with different approaches for liquid injection modelling, including the LISA (Linearized Instability Sheet Atomization) model and the TAB (Taylor Analogy Breakup) model. When used, they account for primary and secondary atomization, respectively.

The LISA model by Senecal et al. [42] includes a general liquid sheet breakup mechanism and a liquid injection methodology specific for pressure-swirl atomizers. The breakup length is given by Eq. (15):

$$L_{bu} = \frac{u_{sheet}}{\Omega_s} \ln\left(\frac{\eta_b}{\eta_0}\right) \tag{15}$$

where Ω_s is the maximum growth rate, derived by a dispersion relation for the sinuous mode of a 2D, viscous, incompressible liquid sheet moving through a quiescent, inviscid and incompressible gas medium. The quantity $\ln\left(\frac{\eta_b}{\eta_0}\right)$ is set to 12 based on the work of Dombrowski and Hooper [43]. Once this sheet breakup length is reached, ligaments and droplets with the diameters given by Eq. (16) and (17) are formed:

$$d_L = C_{LISA}\frac{2\pi}{K_s} \tag{16}$$

$$d_D = 1.88 d_L (1 + 3Oh)^{1/6} \tag{17}$$

where C_{LISA} is a model constant and K_s is the wavenumber corresponding to Ω_s. The model assumes that the injector exit velocity profile is uniform with the total velocity of the sheet parcels given by Eq. (18):

$$u_{sheet} = \max\left[0.7\sqrt{\frac{2\Delta p}{\rho_l}}, \frac{4\dot{m}_l}{\pi d_0^2 \rho_l \cos\theta}\right] \tag{18}$$

where d_0 is the injector exit diameter and θ is the spray angle. The sheet parcel's radius is assumed to be half of the liquid sheet thickness, which in turn is obtained by mass conservation from $\dot{m}_l$ and u_{sheet}.

When used alone or in combination with the LISA model, the TAB model calculates drop distortion and breakup based on the Taylor's analogy between an oscillating and distorting droplet and a spring-mass system, reaching Eq. (19) for the drop distorsion [44]:

$$\ddot{y} = \frac{C_F}{C_b}\frac{\rho_g}{\rho_l}\frac{|u_g - u_{l,i}|^2}{r_0^2} - \frac{C_k\sigma}{\rho_l r_0^3}y - \frac{C_{d,TAB}\mu_l}{\rho_l r_0^2}\dot{y} \tag{19}$$

where r_0 is the drop radius prior to breakup. The default constants from CONVERGE [45], determined by matching experimental and theoretical results [46], have been used in the present investigation: $C_F = 1/3$, $C_b = 1/2$, $C_k = 8$ and $C_{d,TAB} = 5$. The temporal solution of Eq. (19) makes use of a computed drop *We*, a droplet breakup time and a droplet frequency. The latter are given by:

$$\frac{1}{t_d} = \frac{C_{d,TAB}}{2}\frac{\mu_l}{\rho_l r_0^2} \tag{20}$$

$$\omega^2 = C_k\frac{\sigma}{\rho_l r_0^3} - \frac{1}{t_d^2} \tag{21}$$

For each time step, depending on the computed results of y, *We* and ω for a given drop, breakup will be possible or not. If breakup occurs, the normal drop velocity normal component and breakup radius are calculated as:

$$u_{l,n} = 0.5 r_0 \dot{y} \tag{22}$$

$$r_{bu} = \frac{r_0}{1 + \frac{4}{3}y^2 + \frac{1}{8}\frac{\rho_l r_0^3}{\sigma}\dot{y}^2} \tag{23}$$

For further details on the TAB breakup model, the reader is referred to the original work by O'Rourke and Amsden [44].

2.2.3. Drop drag

As seen in Eq. (12), drop drag is quantified by the drag coefficient C_D. For thin sprays considering spherical drops, it can be estimated as a function of the drop Reynolds number (Re_d) [47]:

$$C_{D,sphere} = \begin{cases} \frac{24}{Re_d}\left(1 + \frac{1}{6}Re_d^{2/3}\right) & \text{for } Re_d \leq 1000 \\ 0.424 & \text{for } Re_d \geq 1000 \end{cases} \tag{24}$$

The drop drag coefficient can be affected at conditions involving high relative velocities, due to the oscillation and distortion of the drops during the breakup process. At such conditions, the oscillation amplitude is considered in the calculations of C_D as given by Eq. (25):

$$C_D = C_{D,sphere}(1 + 2.632y) \tag{25}$$

Consequently, in the limit of no drop distortion ($y = 0$) C_D corresponds to that of a spherical drop. At maximum distortion levels ($y = 1$), in turn, the computed drag coefficient corresponds to that of a disk.

2.2.4. Drop turbulent dispersion

The effects of the turbulent flow on the dispersion of spray drops are predicted through a stochastic tracking method. Such approach adds an instantaneous fluctuating velocity $\boldsymbol{u}_i'$ to the gas velocity $\boldsymbol{u}_i$ in the particle trajectory before the integration of Eq. (12). Besides, source terms are included in the LES sub-grid scale model to account for the decrease of turbulent kinetic energy as a consequence of the work done by turbulent eddies to disperse the liquid spray droplets in a parcel:

$$S_s = -\frac{\sum_p N_p\left(F_{D,i}'|\boldsymbol{u}_i'|\right)_p}{V_c} \tag{26}$$

where the summation is performed over all the parcels in the cell, N_p is the number of drops in a parcel, V_c the cell volume and $F_{D,i}'$ is given by:

$$F_{D,i}' = -\frac{F_{D,i}}{|\boldsymbol{u}_i' + \boldsymbol{u}_i - \boldsymbol{u}_l'|}|\boldsymbol{u}_i'| \tag{27}$$

The O'Rourke turbulent dispersion model used in this study assumes that each component of $\boldsymbol{u}_i'$ follows a Gaussian distribution given by Eq. (28):

$$G\left(u'_{i,k}\right) = \frac{1}{\sqrt{2\pi\sigma}} e^{-\frac{1}{2}\left(\frac{u'_{i,k}}{\sigma}\right)^2} \tag{28}$$

with a variance $\sigma^2 = 2/3k$ [48]. The cumulative distribution function for Eq. (28) is given by:

$$\tilde{G}\left(u'_{i,k}\right) = \text{erf}\left(\frac{u'_{i,k}}{\sqrt{4/3k}}\right) = \text{erf}\left(\zeta\right) \tag{29}$$

Newton's method is used to numerically obtain the specific values of $\tilde{G}$ through the inversion of Eq. (29). These values are calculated once at the start of the simulation and stored in a table. When a value of ζ is needed for a turbulent dispersion calculation, a random number between 0 and 1 is selected representing $\tilde{G}$. Then, the corresponding value of ζ is found by interpolating in the table and the associated $u'_{i,k}$ is computed.

The trajectory of each liquid drop is integrated according to the above procedure with the turbulent velocity field of the carrier phase, until a turbulence correlation time t_d is reached and the drop leaves behind the eddy. This drop-eddy interaction time is defined as the lesser of the eddy breakup time (i.e. eddy characteristic lifetime) and the time taken by the droplet to travel across an eddy [49]:

$$t_d = \min\left[\frac{k}{\varepsilon}, C_{ps}\frac{k^{3/2}}{\varepsilon}\frac{1}{\left|\boldsymbol{u}'_{\boldsymbol{i}} + \boldsymbol{u}_{\boldsymbol{i}} - \boldsymbol{u}'_{\boldsymbol{l}}\right|}\right] \tag{30}$$

where C_{ps} is an empirical constant set to 0.03.

2.2.5. Drop collision and coalescence

The O'Rourke collision and coalescence model [50] is used in this study. It considers a stochastic estimation of collisions and assumes that parcels can collide only if they are placed in the same Eulerian cell. CONVERGE performs a collision calculation for a pair of parcels. The collision frequency of a collector drop is calculated by:

$$\nu_{coll} = \frac{N_2\pi\left(r_1 + r_2\right)^2 u_{rel}}{V_c} \tag{31}$$

where N_2 is the number of drops in the droplet parcel. The probability that the collector collides with drops is described by a Poisson distribution whose mean value is $\overline{n} = \nu_{coll}\Delta t$. It may be noted that this is the ratio of the collision volume (collision area multiplied by the distance travelled by a droplet in one time-step) to the Eulerian cell volume, generalized by the number of droplets in the parcel. The O'Rourke model includes two collision outcomes, namely coalescence and grazing collision. For further details on the model, the reader is referred to the original reference [50].

It must be noted that the benefits of using the parcel approach are clearly seen in the light of the need for a drop collision model: the number of possible collision pairs scales with the square of the number of drops. Thus, computations of individual droplet collisions for the whole duration of the simulation are computationally unaffordable.

2.2.6. Drop evaporation

The rate of change in the drop radius $\dot{r}$ shown in Eqs. (9), (10) and (11) due to vaporization is expressed according to the Frossling correlation [48]:

$$\dot{r}_d = -\frac{\rho_g D_f B Sh}{2\rho_v r_d} \tag{32}$$

where the mass transfer number B is related to the fuel mass fraction as:

$$B = \frac{Y_v^* - Y_v}{1 - Y_v^*} \tag{33}$$

where Y_v^* is the vapor mass fraction at the drop surface whereas Y_v represents the vapor mass fraction in the computational cell. The Sherwood number Sh can be written as follows:

$$Sh = \left(2 + 0.6Re_d^{1/2}Sc^{1/3}\right)\frac{\ln(1+B)}{B} \tag{34}$$

where Sc is the Schmidt number of the gas-phase and the last term is the Spalding function to consider the heat transfer modification in turbulent boundary layers. The partial pressure of fuel vapor can be assumed to be equal to the equilibrium vapor pressure, so that the fuel mass fraction at the drop surface is given by Eq. (35):

$$Y_v^* = \frac{W_v}{W_v + W_g\left(\frac{p_g}{p_v T_d} - 1\right)} \tag{35}$$

where W_v and W_g are the vapor and gas molecular weights, whereas p_v and p_g are the vapor and air pressure, respectively.

The time rate of change in drop temperature introduced in Eqs. (7) to (11) can be obtained from an energy balance:

$$\rho_l\frac{4}{3}\pi r_d^3 c_l \dot{T}_d - \rho_l 4\pi r_d^2 \dot{r} l_v = 4\pi r_d^2 \dot{Q}_d \tag{36}$$

where l_v is the specific latent heat for vaporisation at constant temperature and $\dot{Q}_d$ refers to the heat flux (rate of heat conduction to the drop) that can be written as:

$$\dot{Q}_d = -\alpha\left(T - T_d\right) \tag{37}$$

α is the heat transfer coefficient, which can be expressed as:

$$\alpha = \frac{Nu}{2r}\lambda_{eff}\frac{\ln(1+B)}{B} \tag{38}$$

where λ_{eff} is the effective thermal conductivity and the Nusselt number Nu is given by the following correlation [51]:

$$Nu = 2 + 0.6Re^{1/2}Pr^{1/3} \tag{39}$$

2.3. Description of the combustor design

The computational investigation has been carried out based on the experimental two-phase flow version of the CORIA LDI burner [52,53], whose 3D model is depicted in Fig. 1. This burner configuration contains four main components: a plenum that tranquilizes the airflow before it enters the swirler, a radial swirler, a square cross-section combustion chamber (100 × 100 × 260 mm) and a convergent exhaust that prevents air recirculation. The combustor employs a radial swirler comprising 18 rectangular (6 mm × 8 mm) channels inclined at 45° with respect to the radial direction, with an inner and outer diameter of 10 and 20 mm, respectively. The swirler creates an external annular swirling air co-flow in the combustion chamber, in which liquid n-heptane is injected through a simplex pressure-swirl atomizer (Danfoss, 1.46 kg/h, 80° hollow cone) located in the centre of the swirler. It is of primary interest to consider the flow across the plenum and swirler blades in the computational domain in order to eliminate any ambiguity in the inflow conditions as the flow dynamics and coherent structures within the combustion chamber are fundamentally characterised by the flow conditions at the exit of the swirler. The axial direction is referred to as the z-axis, corresponding to the main flow direction, while the x-axis and y-axis denote the transverse directions.

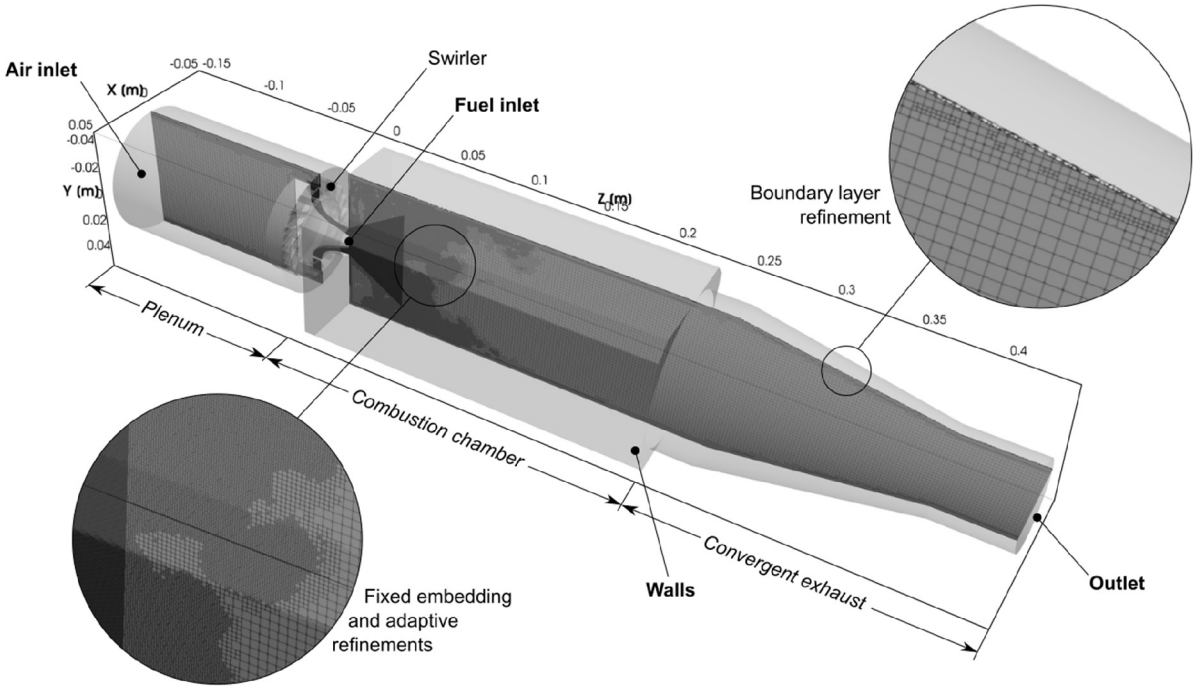

Fig. 1. Global view of the CORIA single burner computational domain and computational mesh illustrating the strategy considered, consisting in 3 levels of fixed embedding in the swirler and injection cone region, 2 levels of AMR, and 2 layers with 2 levels of wall refinement.

Table 1
Operating and boundary conditions.

Magnitude	Value
p [atm]	1
Plenum injection, $\dot{m}_{air}$ [g/s]	8.2
Central injection, $\dot{m}_{C_7H_{16}}$ [g/s]	0.33
Equivalence ratio [–]	0.61
T_{air} [K]	416
$T_{C_7H_{16}}$ [K]	350
T_{wall} [K]	387
U_{bulk} [m/s]	70
$\overline{Re}$ [–]	50,000

2.4. Combustor operating and boundary conditions

In this work, a liquid spray injection strategy has been simulated at atmospheric pressure ($p = 1$ atm). The operating condition corresponds to ultra-lean conditions, for which experimental data are available in the literature [52–55]. Relevant parameters are gathered in Table 1.

As far as the boundary conditions are concerned, the air mass flow rate is prescribed at the air inlet, whereas a constant pressure is prescribed at the outlet. A no-slip boundary condition is used for all the physical walls. Meanwhile, the O'Rourke and Amsden heat transfer model [50] has been employed as a law-of-the-wall temperature boundary condition to set the temperature value at the cell next to the wall by estimating the local fluid-wall heat transfer.

Fuel is injected from the tip of the atomizer (see Fig. 2) with the liquid mass flow rate and temperature imposed according to the experimental operating conditions mentioned above. Moreover, experimental velocity and drop size results from PDA measurements [52–55] taken at 15–35 mm from the nozzle tip have been used to set the spray conditions in the model. From here, two different liquid injection modelling strategies are tested:

- **LISA-TAB case**. The liquid injection and primary atomisation is modelled using the LISA injection-atomisation model [42,56], whereas the TAB breakup model [44] is considered for secondary atomisation. In this way, the hollow cone overall angle is set as 76° with a thickness of 8° (i.e., outer angle 80° and inner angle 72°), whereas the velocity of the injected sheet parcels is initialised from the experimental injection pressure $p_{inj} = 11$ bar.
- **TAB case**. In this case, primary atomisation is not considered. Lagrangian fuel parcels are directly injected according to a Rosin-Rammler distribution characterised by a Sauter Mean Diameter $D_{32} = 31$ µm and a width parameter $q = 2.3$, corresponding to a fitting of the experimental data close to the nozzle, but where secondary atomisation already dominates [52–55]. In this case, the hollow cone overall angle is also set to 76° with a thickness of 8°, but the velocity of the injected sheet parcels is defined through the nozzle diameter in order to match the experimental results. Parcels will then evolve according to the TAB breakup model for secondary atomization.

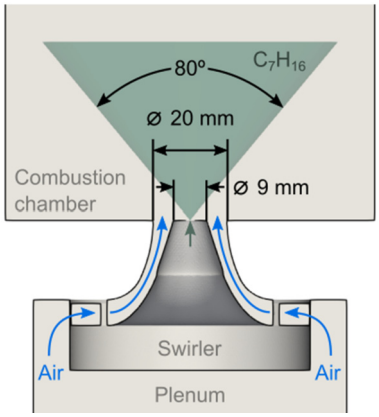

Fig. 2. Sketch of the swirl-injection system showing the liquid spray injection strategy.

The number of total injected parcels has been set according to a sensitivity analysis existing in the literature [57] in order to ensure that all the possible droplet sizes are represented by at least

one parcel. This can be done by dividing the total mass flow rate (0.33 g/s) by the mass of the biggest droplet reported experimentally (75 µm), leading to a number of 3 million parcels/s.

2.5. Meshing strategy

The meshing strategy employed here is adapted from a previous work [27] where the authors defined a methodology to establish a mesh as a compromise between spatial resolution and computational cost in order to work out this multi-scale problem. An automatic domain decomposition technique is employed, allowing for efficient load balancing throughout the calculation. In this regard, the three-dimensional domain is discretized in a structured grid of hexahedrons with a base cell size of 2 mm. To ensure an accurate prediction of the flow behaviour, the cell size is reduced in areas where a finer resolution is critical to the accuracy of the solution (i.e., the flow behaviour within the small passages of the swirler and the spray region), by applying a grid-scale factor (f_{grid}), according to:

$$L_{scaled} = \frac{L_{base}}{2^{f_{grid}}} \tag{40}$$

Following the conclusions extracted in the mentioned mesh methodology, a scale factor of three is applied as fixed embedding (i.e., fixed refinement at user-specified locations and times) to the swirler and a conical near-nozzle region (see Fig. 1). Additionally, another scale factor of two is applied in the adaptive mesh refinement algorithm (AMR) to increase the spatial resolution where velocity gradients are significant (see Fig. 1). In this respect, AMR of y^+ was also used to maintain the proper level of mesh near the wall ensuring y^+ values between 30 and 100 so that the employed Werner and Wengle wall model [58] (whose use was justified in a previous work [27]) can work in a satisfactory way. The total number of cells depends on the simulation timing and varies among 11.5 and 13 million.

2.6. Numerical algorithms

As derived from previous works [34], a second-order-accurate discretisation scheme is used both for the governing conservation equations and the temporal advance. In the same way, the Rhie-Chow algorithm [59] is employed to prevent spurious oscillations (e.g., checker-boarding) and the PISO algorithm is used to solve the transport equations. A variable time-stepping algorithm is used in the current study, where the time-step is automatically calculated each computational cycle based on a maximum allowed CFL number for convection of 0.8.

The solver uses a fully implicit liquid-gas momentum coupling approach in order to keep the simulations stable in the presence of small cells and high liquid volume fractions. A Taylor series expansion is applied in an iterative algorithm where drag is calculated for all parcels in a cell, and the gas-phase velocity is updated accordingly. Then, this updated gas-phase velocity is used to compute drag on all the parcels in the cell, which is again used to update the gas-phase velocity until it converges to the specified tolerance. The variable time step sizes resulting from the CFL restriction mentioned above are between $1.5 \cdot 10^{-6}$ s–$2.5 \cdot 10^{-6}$ s, the mean CFL number being around 0.001.

Fig. 3 sketches the timeline of the simulation events, where τ is defined as the time for one revolution of the Precessing Vortex Core (see discussion later). A mesh scaling of twice the baseline mesh size was used to stabilise the flow field until the simulation time reaches $t/\tau = 50$, where the cell size is automatically scaled down to the base mesh size and the fixed embedding in the swirler region and the use of AMR tools start. The simulations were run for additional $t/\tau = 100$ to stabilise the overall gaseous mass flow rate and velocity fields (i.e., the parameters considered for checking the convergence in a statistical steady state). From this point, liquid injection starts (the additional fixed embedding in the conical near-nozzle region is applied starting $t/\tau = 5$ before the injection). The simulation was then run for additional $t/\tau = 30$ to stabilise the flow and spray field with the final mesh strategy before computing temporal averages and higher-order moments. After this initial transient, approximately 20 τ of data are statistically averaged.

3. Numerical results: validation and discussion

3.1. Flow visualisation

An in-depth analysis of time-evolving structures in the combustor is required in order to achieve a greater insight into the unsteady spray interactions with the turbulent shear layers and the following mixing of the vaporized fuel as well as the effect of breakup in the near-injection region. The characteristic flow patterns present in LDI combustors depend on the geometrical aspects of the swirler and combustion chamber and on the operating conditions. A complete analysis of the time-evolving flow features in the burner and a close examination of the flow near the vicinity of the injection system for a gaseous-fuel case can be found in previous works by the authors [27,34]. Since the same combustor geometry (with slight changes in the airflow rate) is used in this study, only a brief visualisation of the unsteady gaseous features is presented here to later explain the nature of spray-turbulence interactions.

The generation of unsteady coherent structures depends mainly on the swirl intensity, defined by the swirl number S_W, which can be expressed according to Eq. (41) as [60]:

$$S_w = \frac{1}{R_{ext}} \frac{\int_0^{R_{ext}} \rho u_z u_\theta r^2 dr}{\int_0^{R_{ext}} \rho u_z^2 r dr} \tag{41}$$

When S_W exceeds a critical value in the swirler outlet region (typically 0.6 in such flows) [61], a phenomenon known as Vortex Breakdown Bubble (VBB) occurs, leading to the formation of a Central Toroidal Recirculation Zone (CTRZ) encompassed by the inner mixing shear layer (see Fig. 4). In the present work, the swirl number evaluated in the injection plane of the combustion chamber is 0.77 [53], implying that the formation of a VBB is expected. The VBB can be described as the formation of a recirculation zone established downstream of the area expansion close to the nozzle exit where negative velocities yield a stagnation region (enabling to hold the flame and shorten its length) with a surrounding 3D spiral flow in the core. Meanwhile, Corner Recirculation Zones (CRZ) are induced between the outer shear layer and the chamber walls by the confinement of the chamber and the abrupt flow development in the cross-section area when entering the combustion chamber. The higher the S_W, the higher the CRTZ region and, consequently, the smaller the CRZ volume. Due to the low-moderate swirl number, the CTRZ in the 2-D cut of Fig. 4 presents a small area in the centre of the combustor compared to the CRZ. Finally, in between both regions, the primary swirled air (SWJ) flows from the swirler outlet to the jet zone along the chamber, being characterised by strong shear layers (presenting a high level of turbulence) interacting with the spray. All these unsteady, asymmetric and highly-3D flow features are influenced by the swirl strength and play an essential role in the spray dispersion in axial and radial directions.

The steady snapshot of the VBB identified in Fig. 4 through an iso-surface of zero mean axial velocity appears as a single continuous and symmetric region presenting swirling mean flow into and

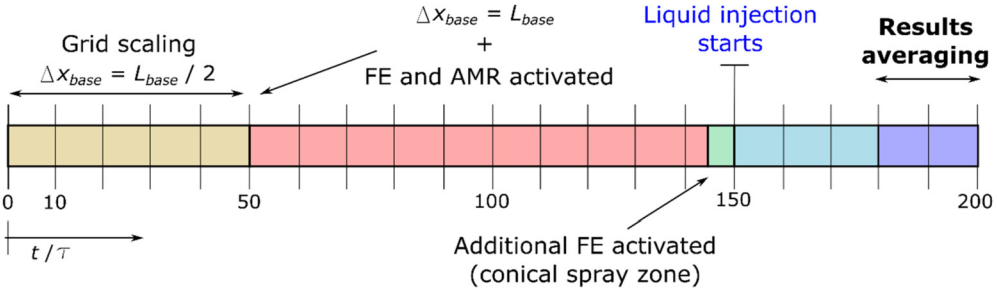

Fig. 3. Sketch of the simulation timeline showing the most relevant events.

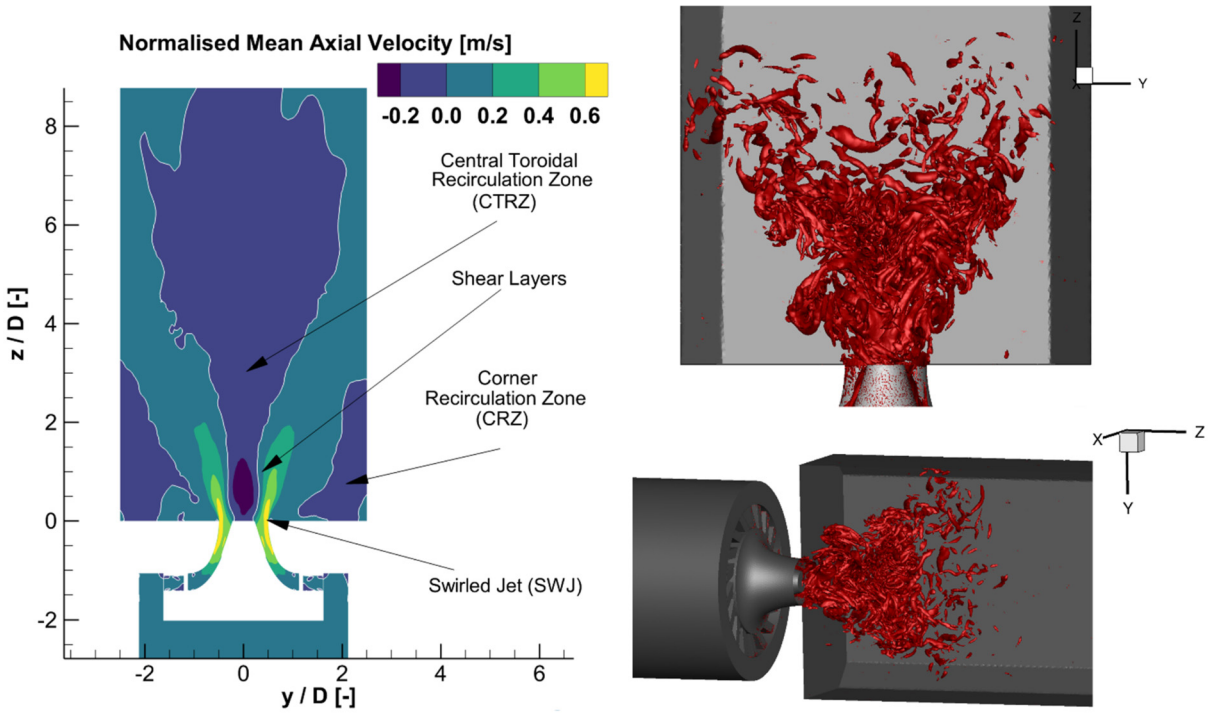

Fig. 4. Left: Mean (time-averaged) axial velocity field in a central x-cut plane showing the characteristic flow pattern within the spray configuration of the CORIA LDI Combustor. White lines represent regions of null axial velocity. Right: Instantaneous visualisation of the PVC structure at 200 ms through an iso-Q criterion contour ($Q = 2 \cdot 10^7$, TAB case).

around it. As it was already found in the previous gaseous-fuelled case study [27], the instantaneous snapshot (not repeated here) is considerably different, presenting unsteady local asymmetry. The Precessing Vortex Core (PVC) originated from the swirler outlet region and essentially dominated by the inflow swirl dynamics is also visualised in Fig. 4, using a Q-criterion iso-surface ($Q = 2 \cdot 10^7$) as a helical-shaped structure rotating around the VBB region.

The coherence of the PVC is sustained for a certain area downstream of the injection plane until it finally dissipates into smaller and less coherent structures (this fact can be better appreciated in temporal evolution records). The rotation time scale associated to the PVC (defined through Eq. (42)) evaluated at the combustion chamber inlet for the liquid-fuelled case investigated here is estimated at $\tau_{PVC} \approx 1$ ms. As will be seen in Section 4.1, this time scale is in fact directly associated to the main modes identified for the PVC.

$$\tau_{PVC} = \frac{2\pi R_i}{u_{\theta,i}} \tag{42}$$

The spray dispersion is strongly governed by the interactions of the spray with the surrounding turbulent gas flow, specifically by the VBB pattern and the rotating motion of the PVC. The LES here presented allows capturing and visualising the instantaneous flow fields, thus accurately predicting the characteristic spiraling motion of the disperse phase in swirling flows accurately. Nevertheless, the spray dispersion (and therefore, the spray-air mixture) can be affected by the breakup modelling as reported in the studies conducted by Patel and Menon [18].

In this way, Fig. 5 shows the visualisation of the spray dispersion under the swirling effect as it evolves in time for the LISA-TAB (top) and TAB (bottom) cases. It can be observed how fuel is injected in a hollow-cone shape to generate a quickly atomised spray and efficient fuel-air mixing downstream of the injector. Spray droplets are forced to a wide radial dispersion because of the increased swirling forces at the shear layer around the VBB. Besides, spray dispersion and mixing is further accentuated a few centimetres downstream of the injection, where randomly oriented structures are generated when the coherence of the PVC breaks down.

In general, the helical Kelvin-Helmholtz instabilities arise from (and synchronise with) the precessing motion of the carrier phase leading the spray both to resemble the spiral PVC pattern (due to the low-pressure inside the structure) and to get confined within the PVC and VBB forming dense pockets of parcels (except for

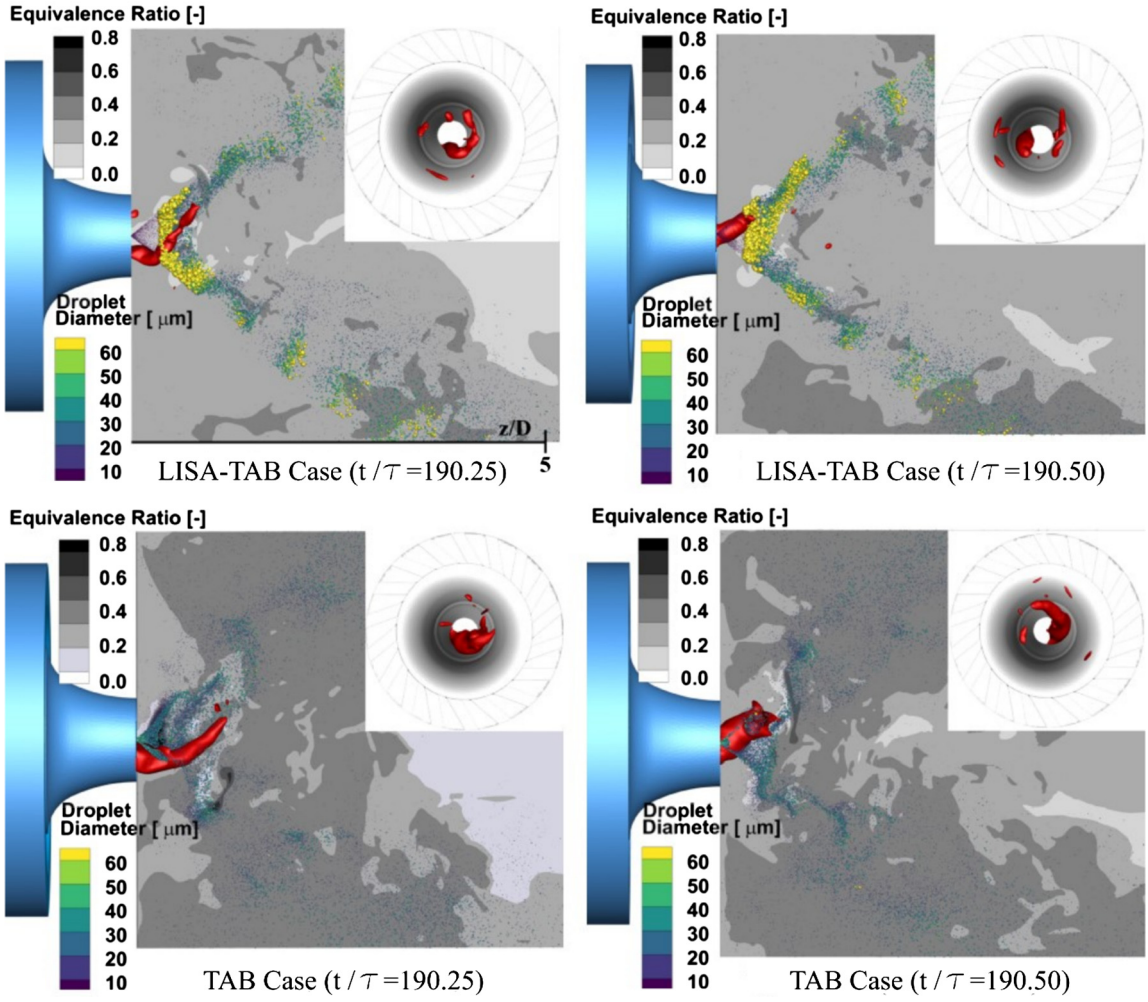

Fig. 5. Representation of the instantaneous parcels, equivalence ratio (dark-coloured) and visualization of the PVC (red) at two instants for LISA-TAB and TAB simulations. The visualisation of the PVC is qualitatively performed through a pressure iso-surface ($p = 100$ kPa) for illustrating purposes, as a Q-criterion visualization would obscure the droplet cloud. (For interpretation of the colours in the figure(s), the reader is referred to the web version of this article.)

parcels presenting large Stokes numbers). This implies the occurrence of high fluctuations in the local fuel concentration [62]. In this way, a high temporal and spatial dependence from the entrainment effect of the PVC on the spray can be established in the form of a spatial correlation between the parcel and PVC positions. Analysis reveals that big parcels ($d > 60$ μm) with high Stokes values travel downstream almost uninfluenced by the local unsteady flow structures in the LISA-TAB Case, due to their inertia (leading to equivalence ratio inhomogeneities); whereas a preferential accumulation of small parcels (low Stokes numbers) is detected around the PVC and captured by the CTRZ in the TAB Case. Such a preferred collection of parcels in low- vorticity regions has been also reported in past studies [18,63]. This fact will be discussed in the following section.

3.2. Mean features

Carrier Phase

The gaseous field resolution was validated in a previous work for the gaseous-fuelled case [27,34]. Therefore, only a brief presentation of gaseous results is here included to confirm the low influence of the fuel spray droplets on the carrier-phase.[1] The axial and tangential components of the numerical time-averaged mean and root-mean-square velocity of the air are plotted in the radial profiles of Fig. 6 at four streamwise locations within the CORIA LDI combustor where PDA air velocity measurements (with no spray) are available in the literature [52–55]. It must be noted that simulation averages are computed from $t/\tau = 180$ to $t/\tau = 200$, i.e. with spray (see Fig. 3). In any case, the influence of the liquid phase on the carrier phase axial and tangential velocity components has been checked to be marginal, as also seen experimentally [52]. Both the mean and RMS velocity profiles obtained from the CFD results show that the computed velocity field is, qualitatively, in good agreement with experiments throughout the four stations. The LES data are able to capture the length and strength of the CTRZ with the correct level of spreading angle, demonstrating the robustness of the numerical methodology and ratifying that the influence of the spray on the air mean velocity is negligible in the near-injection region and thus in the entire combustor.

The deviations among CFD and experimental data have been quantitatively evaluated in the shape of the normalized mean square error (hereinafter referred to as NMSE), defined by Eq. (43):

$$NMSE = \frac{(X_N - X_E)^2}{|X_N X_E|} \tag{43}$$

where X_N is the numerical mean (time-averaged) or RMS value of a given flow variable calculated through CFD in a given spa-

[1] Only one case is here presented since gaseous phase results in LISA-TAB and TAB cases are virtually identical.

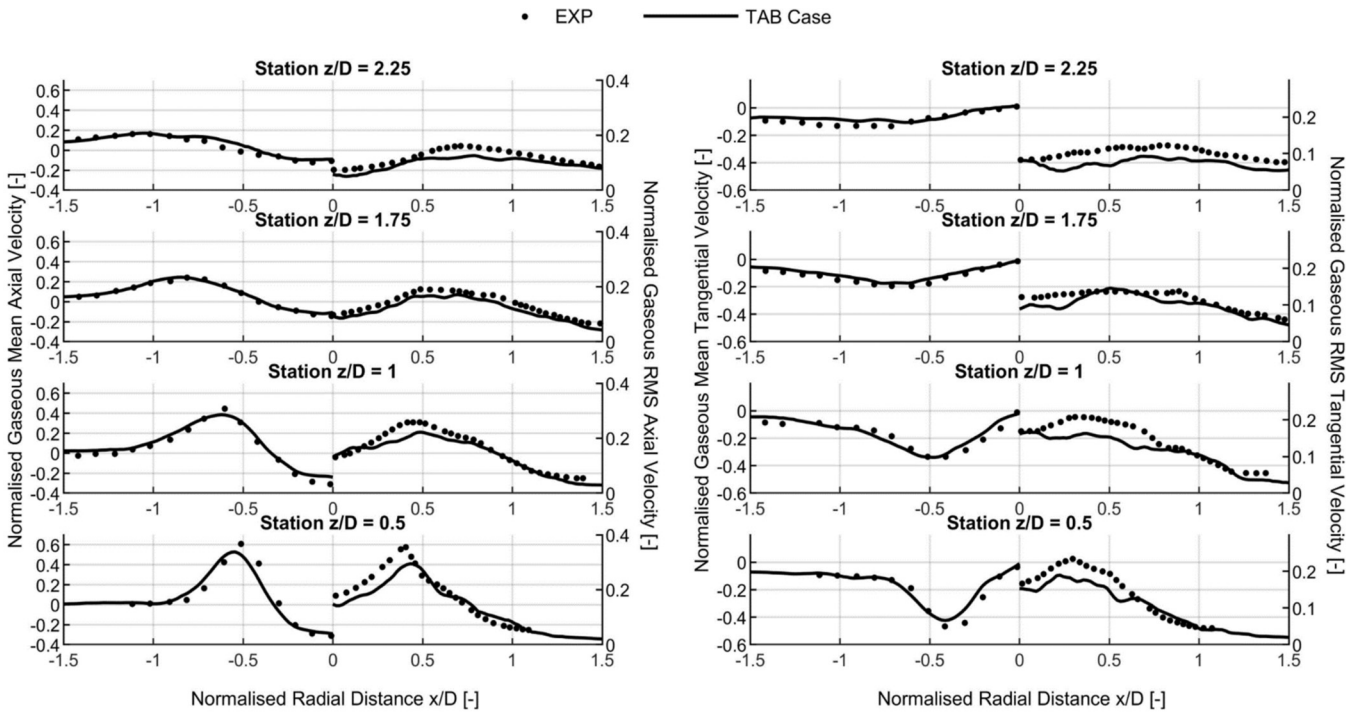

Fig. 6. Mean and RMS axial (left) and tangential (right) velocity profiles obtained for the carrier phase in the TAB case computed from $t/\tau = 180$ to $t/\tau = 200$ (lines) compared against gaseous experiments without spray [52–55] (dots) at four axial locations. Velocity values are normalised with the mean bulk velocity at the swirler exit ($\overline{U}_{ref} = 70$ m/s).

Table 2
NMSE values obtained for each velocity component of the carrier phase.

	$NMSE_{Mean}$	$NMSE_{RMS}$
Axial velocity	0.2055	0.0818
Tangential velocity	0.1286	0.1048
Radial velocity	0.495	0.1091

tial location, and X_E is the corresponding experimental value. A perfect match with experiments would imply $NMSE = 0$, whereas reference studies [64] establish $NMSE < 4$ as an acceptable quality criterion for a predictive model. In this investigation, the values of *NMSE* obtained at each location where experimental data is available have been in turn averaged to synthesize the data in two parameters for each velocity component: $NMSE_{Mean}$ (spatial average of the *NMSE* calculated for the mean data) and $NMSE_{RMS}$ (spatial average of the *NMSE* calculated for the RMS values).

Table 2 shows the *NMSE* values obtained for the validation of the carrier phase. Acceptable values are obtained in all cases, the highest deviation among simulation and experiments been observed for the radial velocity component of the gaseous flow.

Analyzing the flow features, the air mean axial velocity depicted on Fig. 6 (left) shows a co-flow peak of $0.6\overline{U}_{ref}$ (i.e., 40 m/s) at $x/D = 0.5$ and $z/D = 0.5$ which is rapidly diffused downstream up to $0.15\overline{U}_{ref}$ at $z/D = 2.25$. This same trend occurs with the negative axial velocity peak of $-0.3\overline{U}_{ref}$ from $z/D = 0.5$ to $z/D = 1$, which then decreases downstream. Meanwhile, the maximum gaseous mean tangential velocity from Fig. 6 (right) reaches a peak of $0.5\overline{U}_{ref}$, denoting a high swirling motion close to the axial component. The RMS of Fig. 6, in turn, show more substantial turbulent axial and tangential velocity fluctuations close to the chamber inlet. Still, an abrupt decay is experienced as the flow moves both radially (towards zones outside the external shear layer of the air jet) and downstream. The different fluctuation profiles among three components (comparison of the radial component is not shown here for brevity) up to $z/D = 1$ indicate the presence of an anisotropic Reynolds stress distribution produced by the strong swirling flow. The fuel/air mixing is enhanced by these energetic velocity fluctuations, and the trajectories of all the droplets (already atomised when entering this region) are strongly influenced by the air motion (see the following section). Both mean and fluctuating air velocities are small in the CRZs so fuel vapour may have more prolonged residence times than in other regions.

Liquid Phase

A more in-depth insight into the near field region, where the breakup model is expected to impact on the spray distribution field, is achieved through the computation of velocity and size droplet statistics. With regard to the liquid velocity field, Fig. 7 compares the drop axial and radial velocity components from the two CFD cases against the available experimental data [52,55]. Liquid mean and RMS velocity profiles (considering the whole drop sizes population) capture the general features, agreeing with PDA data trends overall. The main discrepancy is the apparent underprediction in the injected spray cone angle at the station $z/D = 0.75$ denoted by the mean axial velocity peak at $x/D = -0.5$, which seems to be recovered further downstream. This difference can be attributed to the slight imprecision in the predicted drop size distribution manifested in Figs. 8 and 9 since both the angle and peak location differs depending on the droplet size, as will be later shown in the velocity-size correlations of Fig. 10. Besides, the LISA-TAB case overpredicts the peak of negative axial velocity of the parcels detected within the CTRZ due to the underprediction in the drop distribution (i.e., the small predicted drop sizes are influenced and accelerated by the reverse gas phase velocity). Meanwhile, the RMS quantities are fully resolved both in TAB and LISA-TAB cases at most axial stations and radial positions but underpredicted in others. Table 3 shows the *NMSE* values obtained for the validation of the liquid phase velocity. Even though the obtained values are larger than those reported for the carrier phase, they meet the criterion of $NMSE < 4$.

The TAB case with the predefined Rosin-Rammler droplet distribution offered the best predicting capabilities in resolving the

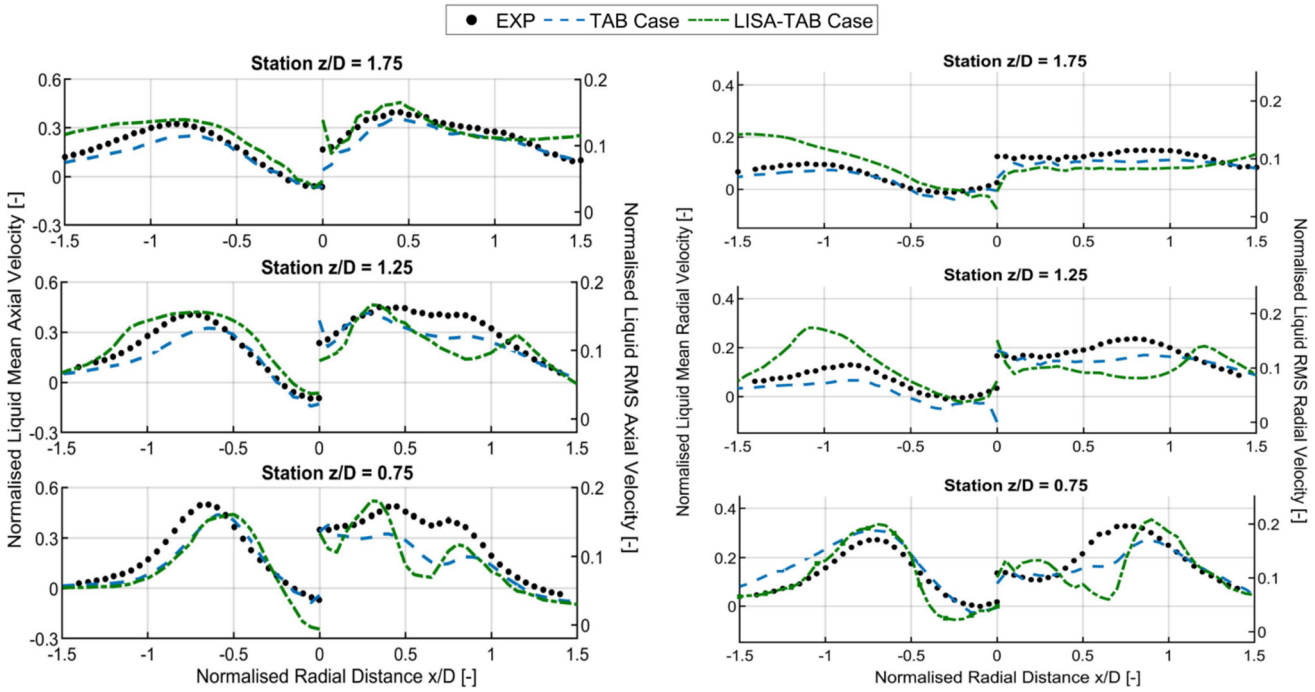

Fig. 7. Mean and RMS axial (left) and radial (right) velocity profiles obtained for the liquid phase in the TAB and LISA-TAB cases (lines) at three axial locations, compared with experimental data [52,55] (dots). Velocity values are normalised with the mean bulk velocity at the swirler exit ($\overline{U}_{ref} = 70$ m/s).

Table 3
NMSE values obtained for each velocity component of the liquid phase.

	$NMSE_{Mean}$	$NMSE_{RMS}$
Axial velocity	0.5593	0.0776
Radial velocity	0.7679	0.0845

liquid velocity field for this particular study, so it will be considered both in the remainder of the section and in the spectral analysis presented in the next section.

An explicit description of droplet size at different axial stations is provided in Fig. 8, where radial profiles of the time-averaged Sauter Mean Diameter (*SMD* or D_{32}) computed by the CFD TAB case are compared against experiments [52], corresponding to a value of $NMSE = 0.8872$. It can be seen how the TAB Case predicts the overall trend and specific sizes along all stations. The larger deviations are found at the most upstream location, where the spray is dense and PDA measurements are known to present more difficulties and uncertainties. Experimental data show bounded profiles with *SMD* values ranging from 23 to 36 µm, where the smallest droplets (those presenting low Stokes numbers) are captured by the VBB and CRZ regions. *SMD* profiles become more uniform at further locations. Meanwhile, the presence of the SWJ pushes the emerging droplets further downstream before completing their breakup processes and thus originating higher *SMD* values at the first axial stations.

A closer examination to the predicted spray size distribution downstream of the nozzle is depicted in Fig. 9. In this way, two histograms are shown at representative locations where PDA data are available [52] (i.e., in the CTRZ -left-, and in the outer edge of the spray cone angle -right-) in order to provide a more detailed characterisation. For each location, the azimuthally averaged number of droplets contained in each parcel per bin size and the sum of droplets across all bins is considered to obtain the probability density function for each group size. Experimental measurements reveal a similar distribution in both locations presenting a locally heterogeneous population with diameters ranging from 5 to

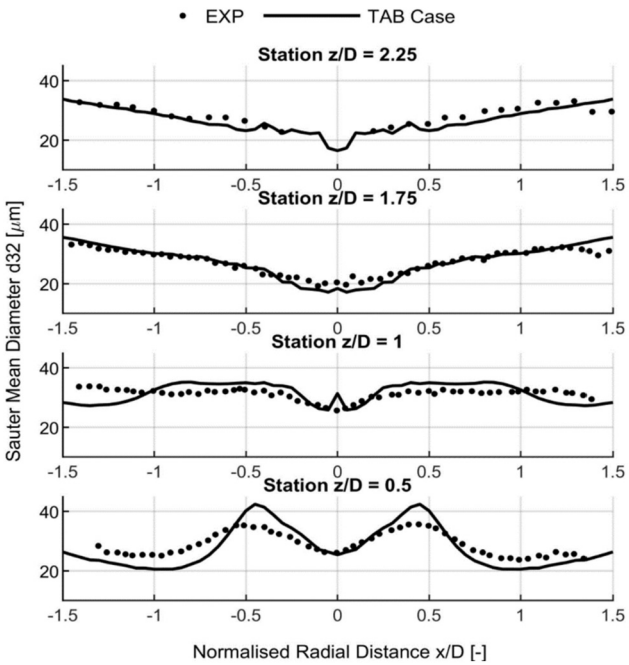

Fig. 8. Sauter Mean Diameter (D_{32}) profiles obtained in the TAB case (lines) at four axial locations, compared with experimental data [52] (dots).

50 µm. Nevertheless, the drop size distributions predicted numerically are narrower. The TAB case is in overall agreement with PDA size distributions, as occurred with the predicted *SMD*. The global trends are respected even when not predicting the exact distribution values: no droplets larger than 40 µm are detected at the CTRZ, while drops up to 60 µm are captured in the SWJ region. Besides, the TAB model can predict that the SWJ contains more droplets ranging from 0 to 15 µm than the CTRZ.

Focusing on the velocity-size correlation, drop velocity components are computed for different groups/bins based on their diam-

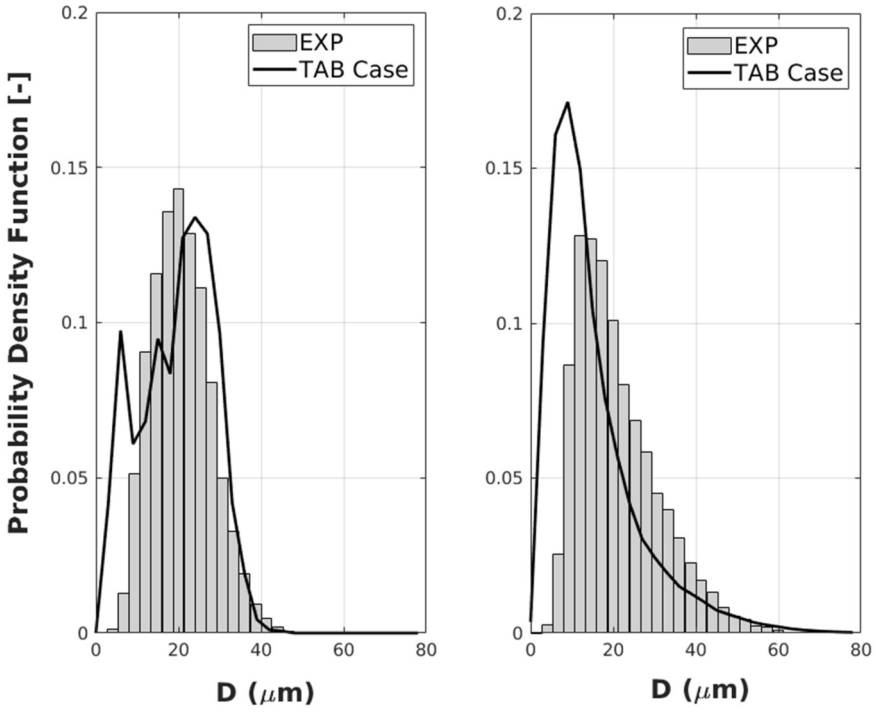

Fig. 9. Particle size distribution obtained in the TAB case at two spatial locations, compared with experimental data [52]. Left: CTRZ ($z/D = 0.5$, $r/D = 0$); Right: SWJ ($z/D = 1$, $r/D = 1$).

eter. Fig. 10 shows the liquid mean and RMS velocity components for the size classes 0–10 μm, 20–30 μm and 40–50 μm corresponding to the TAB case together with the available experimental data. In general, the time-averaged and fluctuating droplet velocity profiles show a reasonable agreement of drop statistics for the three considered bin sizes, thus confirming the success achieved by the Lagrangian tracking approach in conjunction with the TAB breakup model.

As a note on the model validation, even though the agreement with experimental data shown along the present Section 3.2 is not perfect, it must be highlighted that the shown discrepancies (not fully attributable to the computational modelling) are not deemed to invalidate the subsequent frequency analysis. A substantially better liquid phase modelling would imply the need for other modelling approaches (such as Interface Capturing or Interface Tracking methods) with lower cell sizes, raising the computational cost in at least an order of magnitude considering the large computational domain considered. Nevertheless, the present validation ensures this methodology allows capturing the trends of the macro structures of the flow with a degree of accuracy that is enough for the modal decomposition techniques to provide reliable results.

Following the description of the liquid phase evolution, the time-averaged streamwise velocities from Fig. 10 (top, left) reveal how the smaller droplets are strongly accelerated by the co-flow in the first millimetres achieving higher axial velocity peaks at $z/D = 0.75$, as anticipated earlier. However, this trend is inverted as moving towards further radial distances, where the axial velocities of the smaller drops are found to decrease rapidly. Besides, both the 3D expansion, the adverse pressure gradients and the drag effect experienced as the spray evolves further downstream decelerate its evolution lowering and normalising the velocity computed for all group sizes. This effect is much more accentuated in the small particles due to their lower inertia and higher interaction (faster momentum equilibrium) with the carrier phase, changing from almost $0.6\overline{U}_{ref}$ at $z/D = 0.75$ to $0.3\overline{U}_{ref}$ at $z/D = 1.75$.

The particle mean radial velocity profiles plotted in Fig. 10 (top, right) reflect how the radial motion of the spray increases with radial distance. The peak of maximum radial velocity decreases again with axial distance because of the 3D expansion. The negative radial velocity of the small droplets for $x/D < 0.75$ indicates how these low-Stokes particles are pushed towards the centreline ($x/D = 0$) and eventually captured by the CTRZ. Larger spray droplets, in turn, are ejected with high significant velocities ($0.3\overline{U}_{ref}$) following more ballistic trajectories.

Meanwhile, the drop mean tangential velocity profiles (Fig. 10, bottom) show the opposite trend than the radial velocities. Here, the smaller drops present higher mean velocity values at low stations and are rapidly adapted to the airflow further downstream to approximately converge to the velocity of the other size groups, as occurred with the other velocity components.

Finally, the root mean square of the fuel droplet velocity components reveal higher fluctuations for the smaller droplets, being the largest strain rates (about $0.25\overline{U}_{ref}$) located at the SWJ core close to the nozzle ($z/D = 0.75$). It should also be noted that axial and radial RMS profiles exhibit about 30% more fluctuations than the azimuthal component, as observed in the carrier phase.

To conclude with the liquid-phase analysis, the relative velocity magnitude between drops and air[2] is displayed in Fig. 11 for the same three bin groups dealt with before. These slip velocities experienced by fuel droplets are of relevance since they control the evaporation process (vapour production and local equivalence ratio) and thus the two-phase combustion in reacting cases. It can be directly observed how small drops (0–10 μm) present lower slip velocity values (i.e., match more strictly the airflow velocity) than large droplets, as expected. The maximum relative velocities are detected on the spray edges ($x/D = 0.5$) at lower axial distances ($z/D = 0.75$) for big droplets reaching values up to $0.4\overline{U}_{ref}$. Sig-

[2] For each location, the air mean velocity has been substracted to the liquid mean velocity.

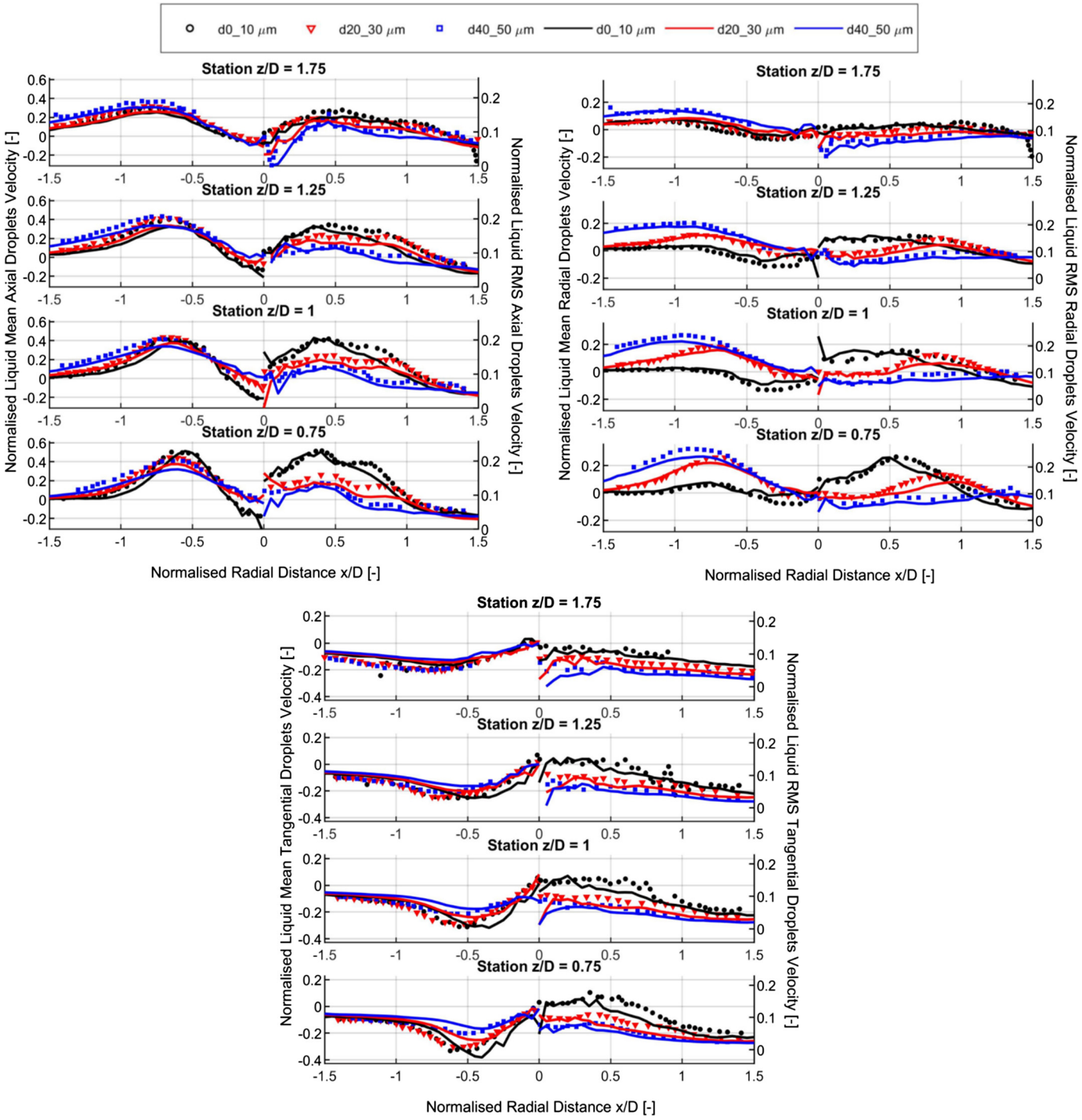

Fig. 10. Liquid Mean and RMS velocity profiles classified by size groups obtained in the TAB case at four axial locations (hollow markers: experimental data [52–54]; lines with filled markers: LES). The three velocity components are depicted: axial (top, left), radial (top, right) and tangential (bottom). Velocity values are normalised with the mean bulk velocity at the swirler exit ($\overline{U}_{ref} = 70$ m/s).

nificant slip velocities are found for the (40–50 μm) group, both close to the centreline and to the nozzle. Meanwhile, once the spray penetrates further downstream the combustion chamber, the slip velocities for the three groups collapse toward values under $0.2\overline{U}_{ref}$. The higher slip velocities of the larger droplets (carrying most of the fuel mass) imply greater evaporation rates, thus contributing to the generation of significant fuel vapour mass. This vapour produced at the spray periphery faces a moderate airflow velocity region with high fluctuations (see Fig. 6) and eventually falls into the CTRZ.

4. Frequency analysis numerical results: validation and discussion

A spectral analysis based on the Proper Othogonal Decomposition (POD) and Dynamic Mode Decomposition (DMD) techniques applied to the 3D pressure and fuel mass fraction fields is performed to the liquid-fuelled TAB Dynamic Smagorinsky LES to shed light and evaluate the specific influence of the dominant PVC on the spray dispersion occurred at the swirler exit region. In this section, special consideration on the relation be-

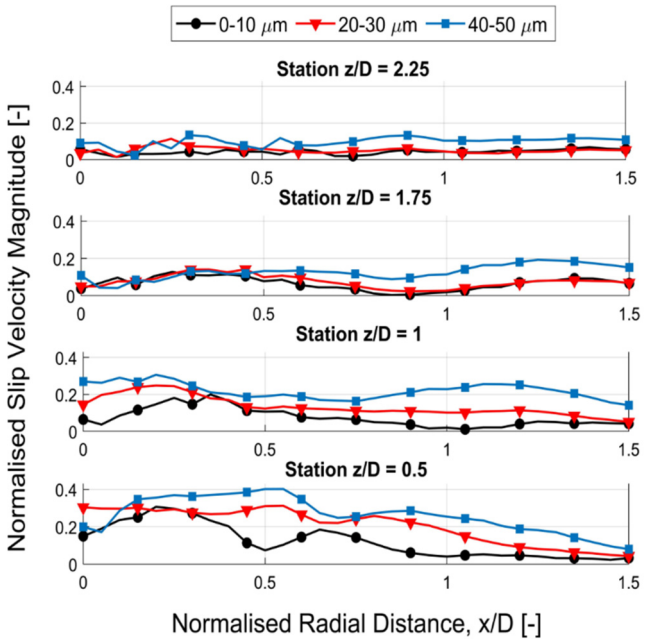

Fig. 11. Liquid-gas mean slip velocity magnitude classified by size groups in TAB case at four axial locations. Velocity values are normalised with the mean bulk velocity at the swirler exit ($\overline{U}_{ref} = 70$ m/s).

tween gaseous structures and liquid fuel propagation is carried out since the theoretical background of both techniques and most of the particularities of the coherent flow structures were discussed in detail in previous studies concerning gaseous-fuelled injections [65,66].

In order to apply the data-driven modal decomposition procedures, the instantaneous pressure and fuel mass fraction fields are exported to text files containing the cell centroid coordinates [**x y z**] and their corresponding static pressures **p** and fuel fractions $\boldsymbol{Y_F}$. For this analysis, a total of 800 snapshots are gathered during a simulated physical time of 20 ms, which implies a spectral resolution of 50 Hz. Data are then exported every 0.025 ms, thus obtaining a sampling frequency of 40 kHz, which is enough to apply the Nyquist criterion in order to isolate the relevant information.

4.1. POD analysis

Proper Orthogonal Decomposition is applied to both the pressure and fuel mass fraction signals in order to identify some correlation between the generation of the main swirling structures from the pressure signal and to determine its effect on the liquid fuel propagation. In this regard, Fig. 12 shows the amplitude of the acoustic[3] POD modes obtained from the 3D pressure (left side) and mass fuel fraction (right side) data, respectively. Furthermore, the spatial distributions of the energetic modes at their identified oscillating frequencies are depicted in Fig. 13. Please note that since the main interest of this study lies on extracting the unsteady structures within the combustor, the first POD mode related to the mean homogeneous pressure and mass fuel fraction can be ignored. Meanwhile, as the operating conditions of the liquid-fuel case originate a tangential velocity at the swirler outlet region of twice the magnitude than the one manifested in the gaseous-fuelled case [66], the rotation time scale associated to a single-helical co-rotating vortex structure (defined through Eq. (3)) evaluated at the combustion chamber inlet for this liquid-fuelled case is estimated at $\tau_{PVC} = 1$ ms (i.e., half of the one manifested in the gaseous-fuelled case), corresponding to a frequency of about 1 kHz (i.e., twice of the one exhibited in the gaseous-fuelled case). Note that the frequency of this acoustic mode would also be slightly higher even if dealing with the same tangential velocity since the air temperature has been increased from 298 K to 416 K, denoting an increase of 14% in the speed of sound.

The characteristic swirling frequency of a single-branched PVC (i.e., 1088 Hz) presenting two different POD modes (modes $\boldsymbol{\Psi_2} - \boldsymbol{\Psi_3}$) with the same associated spectrum is confirmed again in Fig. 12. Such pair of modes are phase-shifted approximately $\pi/2$ rad both in time and space (see Fig. 13), as occurred in the gaseous-fuelled case [66]. Nevertheless, the intermittent emergence and disappearance of the second branch structure (i.e., modes at 2176 Hz: $\boldsymbol{\Psi_5} - \boldsymbol{\Psi_6}$ in Fig. 12 -left- and $\boldsymbol{\Psi_4} - \boldsymbol{\Psi_5}$ in Fig. 12 -right-) associated to the hydrodynamic system is much weaker than the one that was reported for the gaseous-fuelled case in

[3] Note that, in the present study, the term *acoustic* is meant to refer directly to the total fluctuations of the pressure fields and not to the acoustic fields that result from splitting the pressure into acoustic and hydrodynamic fluctuations. This is reasonable since acoustic propagation to a possible far-field is not an objective of this internal flow case with no combustion where the focus is put instead into the hydrodynamic-driven macro structures.

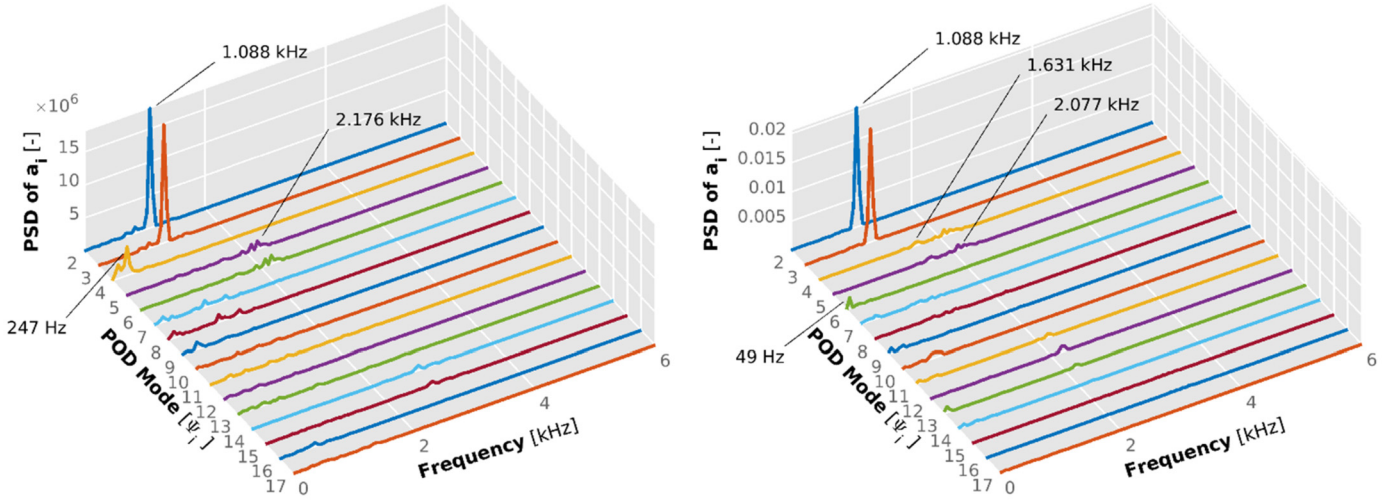

Fig. 12. Power Spectral Density of the time coefficient associated to POD modes $\boldsymbol{\Psi_2} - \boldsymbol{\Psi_{17}}$ obtained from the 3D pressure (left) and fuel mass fraction (right) signals in the frequency domain.

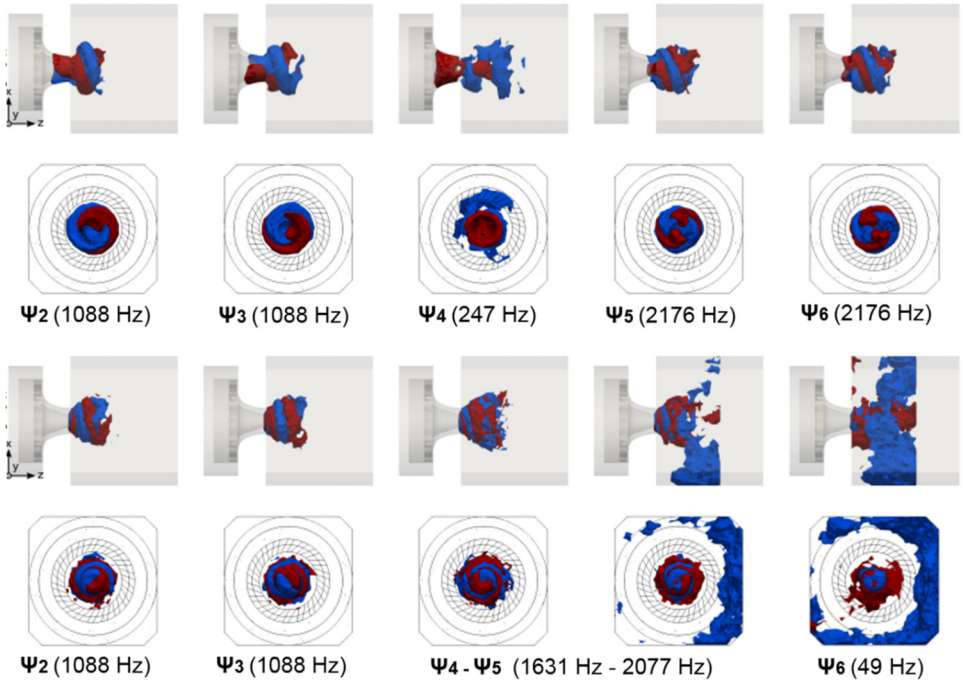

Fig. 13. Spatial distribution of the first five pressure (top) and fuel (bottom) POD modes $\Psi_2 - \Psi_6$ within the combustor. Each mode is represented by iso-surfaces indicating the 2% (red) and 98% (blue) percentiles of the spatial energy distribution of the real values of each mode.

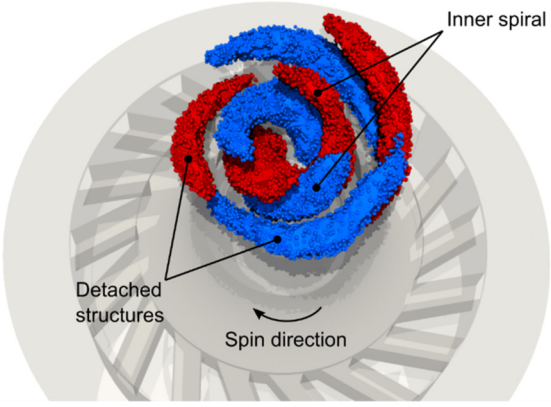

Fig. 14. Spatial distribution of the two-branched pressure POD mode Ψ_6.

the previous work by the authors [66] and other gaseous-fuelled cases in the literature [67], and thus its associated energy content becomes practically unidentifiable in the liquid-fuelled case when compared to the single helical instability. This is one of the most important findings of the present investigation. In fact, the detection of the double helical mode in experimental studies has been reported to be very rare and highly sensitive even to small disturbances [68–70]. For this reason, a more-detailed view of the unusual two-branched mode is shown in Fig. 14. Besides, an intermediate frequency of around 1631 Hz is captured and attributed to these POD modes as a result of an eventual reduction on the rotation velocity of the second branch: both helices start separated by an angular distance of about π rad, but this gap is progressively reduced up to a given instant in which the main branch reaches and encompasses the secondary one. This complex coupled phenomenon has not been captured experimentally and therefore not explained yet, not even in the most recent studies reporting on a possible double helical motion [71–74]. Meanwhile, some low frequency hydrodynamic instability modes (Ψ_6 in Fig. 13 -right-) seem to be captured at 50 Hz, corresponding to leaking effects from the spectral resolution and the gradual slow diffusion of the fuel filling the combustion chamber, without any special physical significance.

Additionally, it is interesting to note how the POD modes of the fuel mass fraction signal present the same dominant frequency peak than the ones extracted from the pressure signal for the spiral breakdown of the single helix PVC ($|m| = 1$). In fact, even the weaker modes ($\Psi_4 - \Psi_5$), related to the double helix PVC ($|m| = 2$), seem to exactly resemble each other for the two predicted pressure frequencies (1631 and 2176 Hz). The high correspondence between the extracted pressure and fuel POD modes is clearly confirmed in the spatial shape representation shown in Fig. 13. Nonetheless, two subtle points should be highlighted here. On the one hand, the POD mode related to the formation of the CTRZ appears to present a higher energy content in the pressure signal spectrum (pressure mode Ψ_4) than the one exhibited for the CTRZ in the mass fuel fraction (fuel mode Ψ_6), thereby indicating a slight delay or impact of the turbulent CTRZ on the fuel droplets capture. On the other hand, the spatial distribution of mass fuel fraction modes $\Psi_4 - \Psi_5$ seems to be more in between single and double helix than in a well-defined double helix, as seen for the pressure signal. This can be explained by the higher peak observed at the intermediate frequency of 1631 Hz by the fuel modes $\Psi_4 - \Psi_5$ in Fig. 12 (right) than the one reported by the pressure modes $\Psi_5 - \Psi_6$ in Fig. 12 (left). Last, it is important to note that modes $\Psi_5 - \Psi_6$ in Fig. 12 (right) seem to be considering some kind of fuel droplets reaching the walls and getting trapped by the corner recirculation zones. This high amount of fuel close to the walls is reasonable since it is a non-reacting case, but has been omitted in the analysis.

Nevertheless, even though the weaker gaseous structures are not observed to have an instantaneous impact on the fuel distribution, a high correlation between the Lagrangian spray dispersion and the Eulerian pressure field has been revealed, specifically with the main coherent structures generated in the near-field of interest. This is an important finding, since this observation suggests (as anticipated from the visualisation of Fig. 5) that it is possible to extract conclusions related to the spatio-temporal characterisa-

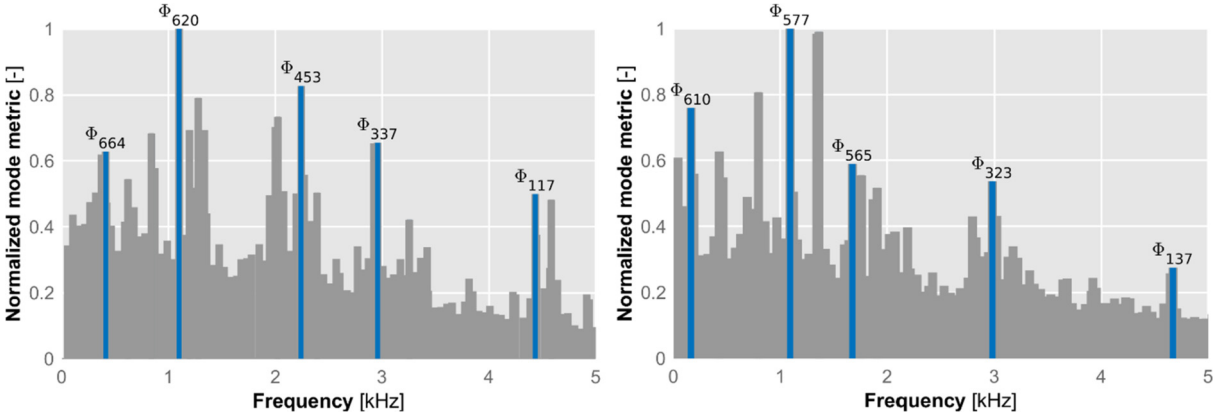

Fig. 15. Normalised relevance $E_i/max_i\ (E_i)$ of the spectrum of DMD modes obtained from the 3D pressure (left) and fuel mass fraction (right) signals.

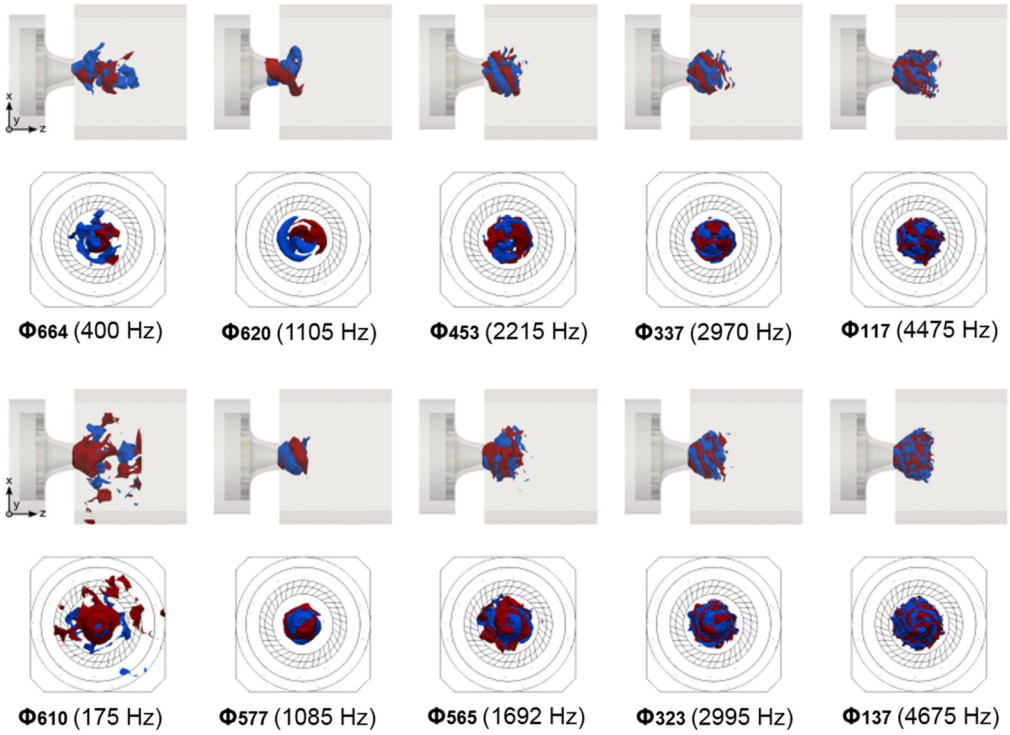

Fig. 16. Spatial distribution of the more coherent pressure (top) and fuel (bottom) DMD modes within the combustor. Each mode is represented by iso-surfaces indicating the 2% (red) and 98% (blue) percentiles of the spatial energy distribution of the real values of each mode.

tion of the liquid-phase by only focusing on the analysis of the pressure data.

4.2. DMD analysis

Finally, the Dynamic Mode Decomposition technique [75] is applied to the numerical spray data to further investigate the spray-turbulence interactions inside the combustion chamber. As previously done with POD, DMD is applied to both the pressure and fuel mass fraction signals to confirm and expand the POD analysis. The relevance E_i of each mode is computed according the normalised Kou & Zhangs's criterion [76] considering the totality of the snapshots. Then, it is normalised with $E_i/max_i\ (E_i)$ to evaluate the relevance of the resulting DMD modes $\mathbf{\Phi_i}$. In this regard, Fig. 15 shows the normalised relevance of the DMD modes according to their associated frequency obtained from the 3D pressure (left side) and mass fuel fraction (right side) data. Furthermore, the spatial distributions of the highlighted coherent and energetic modes at their identified oscillating frequencies are depicted in Fig. 16.

The behaviour shown in Fig. 16 evidences and confirms how the swirl-acoustic interactions led in the VBB and PVC oscillations play a crucial role in the way the fuel spray is internally forced by the PVC wavemaker travelling downstream the swirler and synchronised with its dominant frequency. In this way, the main single-branched PVC mode at 1105 Hz (i.e., $\mathbf{\Phi_{620}}$ in the pressure signal) arises again as the most coherent flow structure, emerging from the swirler and getting twisted as soon as it enters the combustion chamber. Meanwhile, the strong analogous mode computed from the fuel fraction signal ($\mathbf{\Phi_{577}}$) seems to be a direct result/consequence from the aforementioned finding, since it presents the same shape but not as wrapped as the pressure mode, starting at the combustion chamber itself.

In addition, it is important to highlight that the intermediate frequency detected in the pressure POD analysis between 1000 Hz and 2000 Hz due to the intermittency between single and double helical PVC branches is not manifested here. The reason is the

Table 4
Main frequencies of the coherent flow structures of the liquid-fuelled case identified using POD and DMD techniques.

Technique	Signal	PVC				CTRZ
		1st harmonic	2nd harm.	3rd harm.	4th harm.	
POD	Pressure	1088 Hz	2176 Hz	–	–	247 Hz
	Fuel	1088 Hz	2077 Hz	–	–	49 Hz
DMD	Pressure	1105 Hz	2215 Hz	2970 Hz	4475 Hz	400 Hz
	Fuel	1085 Hz	1692 Hz	2995 Hz	4675 Hz	175 Hz

fact that DMD forces the grouping of coherent spatial flow features into modes of a single temporal frequency. In this way, the two different frequencies that were attributed to a single POD mode are here split, isolating and attributing the effects to a well-defined double-helical PVC rotating at 2215 Hz (pressure mode $\mathbf{\Phi_{453}}$). Nevertheless, according to the mass fuel fraction spectrum of Fig. 15 (right), the spray distribution can be affected by this intermittency between single and double helical branches of the PVC, thus leading to the detection of intermediate frequencies between the two associated values even in DMD results (fuel mode $\mathbf{\Phi_{565}}$ at 1682 Hz in Fig. 15 -right-) but without presenting a clear predominant spatial distribution (see Fig. 16). This intermediate DMD frequency in the fuel signal is consistent with the higher peak at the intermediate frequency (1631 Hz) reported on the mass fuel fraction POD analysis of Fig. 12 (right) when compared with the pressure POD spectrum of Fig. 12 (left).

An additional fact that draws attention is how the higher intermittency of the second branch (i.e., the higher amount of simulated time at which the second branch is present) can also lead to more distorted harmonics. Since these harmonics are a result of both the frequency of the main single-branched mode (multiples of 1105 Hz) and the double-branched mode (multiples of 2215 Hz), some mixture and blur in both the resulting frequencies associated to the harmonics and their spatial distribution can be found (mainly in the fuel mass fraction modes) due to this intermittency. In this regard, it can be observed how the pressure mode at 2970 Hz ($\mathbf{\Phi_{337}}$), corresponding to the third harmonic of the main pressure mode ($\mathbf{\Phi_{620}}$), clearly shows three well-defined branches. Meanwhile, the fuel mode at practically the same 2995 Hz ($\mathbf{\Phi_{323}}$) only presents two branches, being more related with the pressure mode at 2215 Hz ($\mathbf{\Phi_{453}}$). Nevertheless, the fourth harmonic at 4675 Hz is able to retrieve the expected four branches both in the pressure ($\mathbf{\Phi_{117}}$) and fuel ($\mathbf{\Phi_{137}}$) DMD modes. Besides, it is interesting to note how the branches seem to be more twisted in the latter, unlike the trend observed in the main mode. This is an important finding, since this observation was not possible using POD.

Finally, in addition to the PVC-like modes, a low-frequency dominant mode on the order of 175 Hz (i.e., $\mathbf{\Phi_{610}}$) is revealed in the DMD spectrum of the mass fuel fraction (see Fig. 15 -right-). The interpretation of its modal structure in Fig. 16 allows the explanation of the trends and suggests that it could be related to the transient shift of the spray edge not being affected by the dominant PVC nor by the shear layers. In fact, DMD studies of experimental liquid injection measurements recently carried out by Leask et al. [77] attributed this low-frequency mode to slow and periodic changes in the spray edge, either in the form of the spray angle increasing and decreasing, or in the form of the spray edge preferentially moving left or right. Besides, the low-frequency DMD mode from the pressure signal (i.e., $\mathbf{\Phi_{664}}$ at 197 Hz) is delimited in a more uniform shape and can be attributed to the generation of a well-defined CTRZ. Note that it presents a higher frequency than the corresponding CTRZ mode presented in the gaseous-fuelled case for the same reason that has been explained at the beginning of Section 4.1. In order to synthesize the results from the techniques and facilitate the comparison among them, the associated frequencies of the main coherent flow structures identified both in the liquid-fuelled and the gaseous-fuelled cases through POD and DMD techniques are compiled in Table 4.

5. Conclusions

An academic LDI gas turbine combustor with a liquid-fuelled injection has been modelled through Dynamic Smagorinsky LES by means of an Eulerian-Lagrangian formulation. The meshing strategy and the SGS model have been selected from a previous work [29] where the authors defined a methodology to define a mesh as a compromise between spatial resolution and computational cost in order to work out this multi-scale problem.

First, the characterisation of the structure of a liquid non-reacting spray immersed in a strong swirling field in the CORIA Spray LDI burner has been determined:

- The relevant phenomena associated to the liquid phase have been modelled, obtaining an overall good agreement with experimental data.
- The capabilities of LISA and TAB breakup models in predicting droplet statistics (e.g., droplet velocity and size distributions) have been assessed. The TAB model together with the Lagrangian tracking formulation has been demonstrated to be able to model the dispersed-phase field within the combustor, obtaining in this particular investigation a better agreement to experimental data than trying to describe primary atomization through the LISA model.
- The fuel spray models have shown to reproduce the overall trends in Sauter Mean Diameter (SMD) and the velocity of the droplets. The shown discrepancies are not deemed to invalidate the subsequent frequency analysis.
- The spray dispersion has been demonstrated to be strongly governed by the interactions of the spray with the surrounding turbulent gas flow, specifically by the VBB pattern and the rotating motion of the PVC.

Once this characterization and validation is performed, the main flow structures generated within the combustor (e.g., Precessing Vortex Core, Vortex Breakdown Bubble, recirculation zones, etc., which play a crucial role in the fuel-air mixing process) have been quantitatively characterised through data-driven modal decomposition techniques such as Proper Orthogonal Decomposition (POD) and Dynamic Mode Decomposition (DMD). These spectral techniques have been applied to the numerical hydrodynamic pressure and spray data to further investigate the spray-turbulence interactions inside the combustion chamber.

The characteristic swirling frequency of a single-branched PVC presenting two different phase-shifted POD modes with the same associated spectrum has been detected. A double-branch mode of the PVC has also been noticed. An important finding is that such double-branch mode of the PVC becomes way less important in the liquid-fuelled case than it had been reported for the gaseous-fuelled case in a previous work, thus explaining why the detection of the double-branch of the PVC has been traditionally more elusive by experimental means.

Besides, DMD analysis has confirmed how the swirl-acoustic interactions led in the VBB and PVC oscillations play a crucial role in the way the fuel spray is internally forced by the PVC wavemaker travelling downstream the swirler and synchronised with its dominant frequency.

Finally, even though the weaker gaseous structures have been observed not to have an instantaneous impact on the fuel distribution, a high correlation has been revealed between the Lagrangian spray dispersion and the Eulerian pressure field, specifically with the main coherent structures generated in the near-field of interest. If this finding were to be confirmed for other cases (with data obtained by other numerical methods or by experimental means) and for more operation and configuration conditions, it would imply that it is possible to extract conclusions related to the spatio-temporal characterisation of the liquid-phase by only focusing on the analysis of the pressure data.

Declaration of competing interest

The authors declare that they have no known competing financial interests or personal relationships that could have appeared to influence the work reported in this paper.

Acknowledgements

This work was partly sponsored by the Spanish Agencia Estatal de Investigación in the frame of the project "Contribución a la aviación sostenible a través de la optimización numérica de cámaras con combustión pobre para aeromotores de nueva generación más silenciosos y limpios (QUILECOM)", reference PID2019-109952RB-I00. We thankfully acknowledge the computer resources at Marenostrum Supercomputer and the technical support provided by Barcelona Supercomputing Center (RES IM-2019-2-0024 and IM-2019-3-0018) in the frame of the Spanish Supercomputing Network. Additionally, the support given to Mr. Mario Belmar by Universitat Politècnica de València through the "FPI-Subprograma 2" grant within the "Programa de Apoyo para la Investigación y Desarrollo (PAID-01-18)" is gratefully acknowledged.

The authors would also like to thank Mr. David Cervelló and Ms. Alicia Muñoz for their technical help and support.

References

[1] ICAO, Doc 10069, Committee on Aviation Environmental Protection, Tenth Meeting, ICAO, Montréal, 2016.
[2] A.H. Lefebvre, D.R. Ballal, Gas Turbine Combustion: Alternative Fuels and Emissions, CRC Press, 2010.
[3] N. Patel, M. Kırtaş, V. Sankaran, et al., Simulation of spray combustion in a lean-direct injection combustor, Proc. Combust. Inst. 31 (2007) 2327–2334.
[4] K. Luo, H. Pitsch, M.G. Pai, et al., Direct numerical simulations and analysis of three-dimensional n-heptane spray flames in a model swirl combustor, Proc. Combust. Inst. 33 (2011) 2143–2152.
[5] V. Sankaran, S. Menon, LES of spray combustion in swirling flows, J. Turbul. 3 (2002), https://doi.org/10.1088/1468-5248/3/1/011, Epub ahead of print 2002.
[6] W.P. Jones, A.J. Marquis, K. Vogiatzaki, Large-eddy simulation of spray combustion in a gas turbine combustor, Combust. Flame 161 (2014) 222–239.
[7] Y. Zhou, C. Zhang, X. Han, et al., Monitoring combustion instabilities of stratified swirl flames by feature extractions of time-averaged flame images using deep learning method, Aerosp. Sci. Technol. 109 (2021) 106443.
[8] S. Menon, N. Patel, Subgrid modelling for simulation of spray combustion in large-scale combustors, AIAA J. 44 (2006) 709–723.
[9] P. Weigand, W. Meier, X.R. Duan, et al., Investigations of swirl flames in a gas turbine model combustor, Combust. Flame 144 (2006) 205–224.
[10] M. Sanjosé, J.M. Senoner, F. Jaegle, et al., Fuel injection model for Euler–Euler and Euler–Lagrange large-eddy simulations of an evaporating spray inside an aeronautical combustor, Int. J. Multiph. Flow 37 (2011) 514–529.
[11] J.A. Colby, S. Menon, J. Jagoda, Spray and emission characteristics near lean blow out in a counter-swirl stabilized gas turbine combustor, in: Turbo Expo: Power for Land, Sea, and Air, Volume 1: Combustion and Fuels, Education, 2006, pp. 753–762.
[12] F. Shum-Kivan, J. Marrero Santiago, A. Verdier, et al., Experimental and numerical analysis of a turbulent spray flame structure, Proc. Combust. Inst. 36 (2017) 2567–2575.
[13] I.A. Mulla, G. Godard, B. Renou, Instantaneous planar measurements of nitric oxide concentration in a turbulent n-heptane spray flame, Combust. Flame 208 (2019) 451–471.
[14] I.A. Mulla, B. Renou, Simultaneous imaging of soot volume fraction, PAH, and OH in a turbulent n-heptane spray flame, Combust. Flame 209 (2019) 452–466.
[15] D. Barré, L. Esclapez, M. Cordier, et al., Flame propagation in aeronautical swirled multi-burners: experimental and numerical investigation, Combust. Flame 161 (2014) 2387–2405.
[16] J. Marrero-Santiago, F. Collin-Bastiani, E. Riber, et al., On the mechanisms of flame kernel extinction or survival during aeronautical ignition sequences: experimental and numerical analysis, Combust. Flame 222 (2020) 70–84.
[17] S. Legros, C. Brunet, P. Domingo-Alvarez, et al., Combustion for aircraft propulsion: progress in advanced laser-based diagnostics on high-pressure kerosene/air flames produced with low-NOx fuel injection systems, Combust. Flame 224 (2021) 273–294.
[18] N. Patel, S. Menon, Simulation of spray–turbulence–flame interactions in a lean direct injection combustor, Combust. Flame 153 (2008) 228–257.
[19] M. Boileau, G. Staffelbach, B. Cuenot, et al., LES of an ignition sequence in a gas turbine engine, Combust. Flame 154 (2008) 2–22.
[20] R-H. Chen, J.F. Driscoll, The role of the recirculation vortex in improving fuel-air mixing within swirling flames, Symp. Combust. 22 (1989) 531–540.
[21] C. Presser, A.K. Gupta, H.G. Semerjian, Aerodynamic characteristics of swirling spray flames: pressure-jet atomizer, Combust. Flame 92 (1993) 25–44.
[22] R. Hadef, B. Lenze, Measurements of droplets characteristics in a swirl-stabilized spray flame, Exp. Therm. Fluid Sci. 30 (2005) 117–130.
[23] M.R. Soltani, K. Ghorbanian, M. Ashjaee, et al., Spray characteristics of a liquid–liquid coaxial swirl atomizer at different mass flow rates, Aerosp. Sci. Technol. 9 (2005) 592–604.
[24] A. Tratnig, G. Brenn, Drop size spectra in sprays from pressure-swirl atomizers, Int. J. Multiph. Flow 36 (2010) 349–363.
[25] M. Sanjosé, E. Riber, L. Gicquel, et al., Large Eddy Simulation of a Two-Phase Reacting Flow in an Experimental Burner, pp. 345–351.
[26] V.R. Hasti, P. Kundu, G. Kumar, et al., Numerical Simulation of Flow Distribution in a Realistic Gas Turbine Combustor, in: 2018 Joint Propulsion Conference, American Institute of Aeronautics and Astronautics, Reston, Virginia, 2018, Epub ahead of print 9 July 2018.
[27] R. Payri, R. Novella, M. Carreres, et al., Modeling gaseous non-reactive flow in a lean direct injection gas turbine combustor through an advanced mesh control strategy, Proc. Inst. Mech. Eng., G J. Aerosp. Eng. 234 (2020) 1788–1810.
[28] M. Boileau, S. Pascaud, E. Riber, et al., Investigation of two-fluid methods for large eddy simulation of spray combustion in gas turbines, Flow Turbul. Combust. 80 (2008) 291–321.
[29] V. Sankaran, S. Menon, Vorticity-scalar alignments and small-scale structures in swirling spray combustion, Proc. Combust. Inst. 29 (2002) 577–584.
[30] D. Caraeni, C. Bergström, L. Fuchs, Modeling of liquid fuel injection, evaporation and mixing in a gas turbine burner using large eddy simulations, Flow Turbul. Combust. 65 (2000) 223–244.
[31] Y. Yan, J. Zhao, J. Zhang, et al., Large-eddy simulation of two-phase spray combustion for gas turbine combustors, Appl. Therm. Eng. 28 (2008) 1365–1374.
[32] M. Chrigui, A.R. Masri, A. Sadiki, et al., Large eddy simulation of a polydisperse ethanol spray flame, Flow Turbul. Combust. 90 (2013) 813–832.
[33] M. Arienti, X. Li, M.C. Soteriou, et al., Coupled level-set/volume-of-fluid method for simulation of injector atomization, J. Propuls. Power 29 (2013) 147–157.
[34] R. Payri, R. Novella, M. Carreres, et al., Study about the influence of an automatic meshing algorithm on numerical simulations of a gaseous-fuelled Lean Direct Injection (LDI) gas turbine combustor in non-reactive conditions, in: ILASS - Europe 2019, 29th Conference on Liquid Atomization and Spray Systems, Paris, France, 2019.
[35] Z. Wang, B. Hu, A. Fang, et al., Analyzing lean blow-off limits of gas turbine combustors based on local and global Damköhler number of reaction zone, Aerosp. Sci. Technol. 111 (2021) 106532.
[36] Z. Rao, R. Li, B. Zhang, et al., Experimental investigations of equivalence ratio effect on nonlinear dynamics features in premixed swirl-stabilized combustor, Aerosp. Sci. Technol. 112 (2021) 106601.
[37] F.A. Williams, Combustion Theory, 2nd ed., CRC Press, Boca Raton, FL, 1985.
[38] J. Smagorinsky, General circulation experiments with the primitive equations, Mon. Weather Rev. 91 (1963) 99–164.
[39] M. Germano, U. Piomelli, P. Moin, et al., A dynamic subgrid-scale eddy viscosity model, Phys. Fluids A, Fluid Dyn. 3 (1991) 1760.
[40] S.B. Pope, Ten questions concerning the large-eddy simulation of turbulent flows, New J. Phys. 6 (2004).
[41] I.B. Celik, Z.N. Cehreli, I. Yavuz, Index of resolution quality for large eddy simulations, J. Fluids Eng. Trans. ASME 127 (2005) 949–958.
[42] P.K. Senecal, D.P. Schmidt, I. Nouar, et al., Modeling high-speed viscous liquid sheet atomization, Int. J. Multiph. Flow 25 (1999) 1073–1097.
[43] N. Dombrowski, P.C. Hooper, The effect of ambient density on drop formation in sprays, Chem. Eng. Sci. 17 (1962) 291–305.

[44] P.J. O'Rourke, A.A. Amsden, The tab method for numerical calculation of spray droplet breakup, in: 1987 SAE International Fall Fuels and Lubricants Meeting and Exhibition, 1987, Epub ahead of print 1 November 1987.
[45] Convergent Science, https://convergecfd.com.
[46] S.H. Lamb, Hydrodynamics, 6th ed., Cambridge University Press, Cambridge, 1994.
[47] A.B. Liu, D. Mather, R.D. Reitz, Modeling the effects of drop drag and breakup on fuel sprays, in: SAE International Congress and Exposition, 1993, pp. 1–6.
[48] A.A. Amsden, P.J. O'Rourke, T.D. Butler, KIVA-II: a computer program for chemically reactive flows with sprays, Los Alamos, NM (United States). Epub ahead of print 1 May 1989, https://doi.org/10.2172/6228444.
[49] C.T. Crowe, J.N. Chung, T.R. Troutt, Particle mixing in free shear flows, Prog. Energy Combust. Sci. 14 (1988) 171–194.
[50] P.J. O'Rourke, Collective Drop Effects on Vaporizing Liquid Sprays, Princeton University, 1981.
[51] W.E. Ranz, W.R. Marshall, Evaporation from drops: part II, Chem. Eng. Prog. 48 (1952) 141–146.
[52] J. Marrero-Santiago, Experimental Study of Lean Aeronautical Ignition. Impact of Critical Parameters on the Mechanisms Acting Along the Different Ignition Phases, INSA de Rouen - Normandie, 2018.
[53] J. Marrero-Santiago, A. Verdier, G. Godard, et al., Experimental study of airflow velocity, fuel droplet size - velocity and flame structure in a confined swirled jet - spray flame, in: ILASS - Europe 2016, 2016.
[54] J. Marrero-Santiago, A. Verdier, C. Brunet, et al., Experimental study of aeronautical ignition in a swirled confined jet-spray burner, J. Eng. Gas Turbines Power 140 (2) (2018) 021502, https://doi.org/10.1115/1.4037752, Epub ahead of print 1 February 2018.
[55] F. Collin-Bastiani, J. Marrero-Santiago, A. Verdier, et al., On the extinction and ignition mechanisms along the ignition events in the KIAI spray burner. A joint experimental and numerical approach, in: S. Tech (Ed.), 4e Colloque du Reseau D'INitiative en Combustion Avancee (INCA), Paliseau, France, 2017.
[56] D.P. Schmidt, I. Nouar, P.K. Senecal, et al., Pressure-Swirl atomization in the near field, in: SAE Paper 1999, 1999, Epub ahead of print 1 March 1999.
[57] D.A. Alessandro, I. Stankovic, B. Merci, LES study of a turbulent spray jet: mesh sensitivity, mesh-parcels interaction and injection methodology, Flow Turbul. Combust. 103 (2019) 537–564, https://doi.org/10.1007/s10494-019-00039-7, Epub ahead of print 2019.
[58] H. Wengle, H. Werner, Large-eddy Simulation of Turbulent Flow over Sharp-edged Obstacles in a Plate Channel, pp. 192–199.
[59] C.M. Rhie, W.L. Chow, Numerical study of the turbulent flow past an airfoil with trailing edge separation, AIAA J. 21 (1983) 1525–1532.
[60] T. Ivanic, E. Foucault, J. Pecheux, Dynamics of swirling jet flows, Exp. Fluids 35 (2003) 317–324.
[61] Y. Huang, V. Yang, Dynamics and stability of lean-premixed swirl-stabilized combustion, Prog. Energy Combust. Sci. 35 (2009) 293–364.
[62] D. Galley, S. Ducruix, F. Lacas, et al., Mixing and stabilization study of a partially premixed swirling flame using laser induced fluorescence, Combust. Flame 158 (2011) 155–171.
[63] C. Yoon, R. Gejji, W. Anderson, Computational investigation of combustion dynamics in a lean direct injection gas turbine combustor, in: 51st AIAA Aerospace Sciences Meeting Including the New Horizons Forum and Aerospace Exposition, American Institute of Aeronautics and Astronautics, Reston, Virigina, 2013, Epub ahead of print 7 January 2013.
[64] S.R. Hanna, O.R. Hansen, S. Dharmavaram, FLACS CFD air quality model performance evaluation with Kit Fox, MUST, Prairie Grass, and EMU observations, Atmos. Environ. 38 (2004) 4675–4687.
[65] M. Carreres, L.M. Garcia-Cuevas, J. García-Tíscar, et al., Spectral analysis of an aeronautical lean direct injection burner through large eddy simulation, Proc. ASME Turbo Expo. 2C-2020 (2020) 1–13.
[66] F.J. Salvador, M. Carreres, J. García-Tíscar, et al., Modal decomposition of the unsteady non-reactive flow field in a swirl-stabilized combustor operated by a Lean Premixed injection system, Aerosp. Sci. Technol. 112 (2021) 106622.
[67] Y. Zhang, M. Vanierschot, Determination of single and double helical structures in a swirling jet by spectral proper orthogonal decomposition, Phys. Fluids 33 (2021) 015115, https://doi.org/10.1063/5.0032985, Epub ahead of print 2021.
[68] T. Sarpkaya, On stationary and travelling vortex breakdowns, J. Fluid Mech. 45 (1971) 545–559.
[69] M.P. Escudier, N. Zehnder, Vortex-flow regimes, J. Fluid Mech. 115 (1982) 105.
[70] P. Billant, J-M. Chomaz, P. Huerre, Experimental study of vortex breakdown in swirling jets, J. Fluid Mech. 376 (1998) 183–219.
[71] J. O'Connor, T. Lieuwen, Recirculation zone dynamics of a transversely excited swirl flow and flame, Phys. Fluids 24 (2012) 075107.
[72] M. Vanierschot, M. Percin, B.W. van Oudheusden, Double helix vortex breakdown in a turbulent swirling annular jet flow, Phys. Rev. Fluids 3 (2018) 034703.
[73] F. Cozzi, R. Sharma, G. Solero, Analysis of coherent structures in the near-field region of an isothermal free swirling jet after vortex breakdown, Exp. Therm. Fluid Sci. 109 (2019) 109860.
[74] M. Vanierschot, J.S. Müller, M. Sieber, et al., Single- and double-helix vortex breakdown as two dominant global modes in turbulent swirling jet flow, J. Fluid Mech. (2020) 883, A31.
[75] P.J. Schmid, Dynamic mode decomposition of numerical and experimental data, J. Fluid Mech. 656 (2010) 5–28.
[76] J. Kou, W. Zhang, An improved criterion to select dominant modes from dynamic mode decomposition, Eur. J. Mech. B, Fluids 62 (2017) 109–129.
[77] S.B. Leask, A.K. Li, V.G. McDonell, et al., Preliminary development of a measurement reference using a research simplex atomizer, J. Fluids Eng. Trans. ASME 141 (2019) 1–11.